Original Article

Institution of MECHANICAL ENGINEERS
Journal of POWER AND ENERGY

Proc IMechE Part A:
J Power and Energy
2021, Vol. 235(5) 1053–1079

Article reuse guidelines:
sagepub.com/journals-permissions
DOI: 10.1177/0957650920909718
journals.sagepub.com/home/pia

Analysis of ultra-low uncertainty gas turbine flow capacity measurement techniques

Daniel Burdett, Chris Hambidge and Thomas Povey

Abstract

Accurate assessment of nozzle guide vane (NGV) capacity is essential for understanding engine performance data, and to achieve accurate turbine stage matching. In accelerated engine development programmes in particular, accurate and early assessment of NGV capacity is a significant advantage. Whilst the capabilities of computational methods have improved rapidly in recent years, the accuracy of absolute capacity prediction capability is lower than experimental techniques by some margin. Thus, experimental measurement of NGV capacity is still regarded as an essential part of many engine programmes. The semi-transient capacity measurement technique, developed and refined at the University of Oxford over the last 10 years, allows rapid and accurate measurement of engine component (typically fully cooled NGVs) capacity at engine-representative conditions of Mach and Reynolds numbers and coolant-to-mainstream pressure ratio. The technique has been demonstrated to offer considerable advantages over traditional (industrial steady-state) techniques in terms of accuracy, time and operating cost. Since the original facility was constructed, the facility has been modularised to allow for rapid interchange of test vane modules, and the instrumentation has been optimised to drive down the uncertainty in NGV capacity. In this paper, these improvements are described in detail, and a detailed uncertainty analysis is presented of the original facility, the current facility, and a proposed future facility in which the uncertainty of the measurement has been driven down to a practical limit. The bias errors of the three facilities are determined to be $\pm 0.535\%$, $\pm 0.495\%$ and $\pm 0.301\%$, respectively (to 95% confidence). The corresponding precision uncertainties are $\pm 0.028\%$, $\pm 0.025\%$ and $\pm 0.025\%$, respectively. The extremely low precision uncertainty in particular allows very small changes in capacity to be resolved. This, combined with rapid interchangeability of test modules, allows studies of the sensitivity of capacity to secondary influences with much greater flexibility than was previously possible. Consideration is also given to the definition of vane capacity in systems with several streams at different conditions of inlet total pressure and temperature. A typical high pressure (HP) NGV has three distinct streams: a mainstream flow; coolant flow ejected from film cooling holes (distributed over the vane surface); and trailing edge coolant ejection. Whilst it is helpful for the coolant mass flow rates and inlet temperatures to be included in the definition, only a relatively small difference arises from the way in which this is achieved. Several definitions appear to share similar usefulness in terms of their robustness to changing inlet conditions of individual streams, but the favoured definition offers the possibility of isolating sensitivities to key effects such as trailing edge coolant ejection. This is achieved by explicitly expressing vane capacity as a function of two controlling pressure ratios. The overall purpose of this paper is to review and analyse in detail the current state-of-the-art in gas turbine flow capacity measurement.

Keywords

Turbomachinery aerodynamics, turbomachinery flow, turbine heat transfer, turbine design, gas turbine cycles, gas turbine performance, gas turbines, gas turbine aerodynamics, engine performance, engine testing, capacity, experimental methods

Date received: 15 August 2019; accepted: 7 January 2019

Department of Engineering Science, University of Oxford, Oxford, UK

Corresponding author:
Thomas Povey, Department of Engineering Science, University of Oxford, Oxford OX2 0ES, UK.
Email: thomas.povey@eng.ox.ac.uk

Introduction

Capacity is commonly defined as

$$\Gamma = \frac{\dot{m}\sqrt{T_0}}{p_0} \tag{1}$$

Although this is not a non-dimensional quantity, the formulation is useful because it removes the primary sensitivities of mass flow rate to total pressure and temperature, and gives a parameter which at choked conditions can be thought of as a crude proxy for effective area. In this formulation, capacity is a function of gas properties, γ and R, and the pressure ratio across the vane, p_{exit}/p_{01}. We can write $\Gamma = f(\gamma, R, p_{\text{exit}}/p_{01})$. The definition of capacity for a fully cooled HP nozzle guide vane (NGV)—and its sensitivity to key operating parameters—is discussed later in this paper.

Accurate assessment of NGV capacity (here we refer loosely to the capacity characteristic of the part, but note that most engines operate on the relatively flat part of the curve at near-choked conditions) is important for both performance (stage matching implications) and power (overall core mass flow rate). The *exchange rate* between capacity and efficiency can be as high as 0.2. Likewise the exchange rate between capacity and engine power is close to unity.

Although high fidelity numerical methods are now deployed routinely for capacity evaluation (fully featured NGV part geometries, with finely resolved meshes), it remains difficult to evaluate vane capacity numerically to high accuracy (better than 1–2%). This is due to the strong dependence of the aerodynamics on features which are at the limit of the process capability to geometrically resolve, and due to inadequacies in the numerical methods.

Errors in the CFD geometry can arise either due to manufacturing variation (real part differs from the casting definition), where the CFD geometry is based on the design CAD, or due to limitations of the scanning process (e.g. by structured light scanning techniques, for example), where the CFD geometry is based on cast parts. Even for processes which use scans of real parts, questions arise regarding how best to clean the geometry (to take it from a cloud of scan points to a clean CAD geometry) and how best to create a part (or parts) from a statistical distribution of geometries. In a high accuracy process, this becomes significant.

Regardless of the method of geometry and mesh generation, elimination of deviations from the real part geometry at a relevant scale for high accuracy capacity evaluation is difficult. To justify this, consider two specific cases. First, the width of the slot formed near the region of minimum area in a modern civil engine is typically of order 10 mm. Hence a 0.1 mm deviation of the numerical mesh from the real part geometry will equate to a capacity discrepancy of order 1%.

Second, consider coolant ejection from a trailing edge slot—either a centred slot, or a slot with a suction side trailing edge overhang. Both configurations are common, with coolant flows up to 2.50% of the mainstream flow.[1] HP NGVs generally operate transonically in this region of the flow path (local Mach number typically in the range 0.8–1.1). The aerodynamic flow field is therefore strongly influenced by the introduction of coolant flow. In particular, the computational method must establish appropriate boundary conditions for the trailing edge coolant slot, and reproduce the geometry with sufficient accuracy. For example, the radius of the trailing edge lands—often dressed by hand—and internal geometry features which define the distribution of coolant flow within the slot. Further, the numerical solver is required to establish the base pressure correctly in a region with three converging high momentum streams (pressure surface, suction surface and trailing edge-coolant jet) separated by four shear layers, in a situation where the underlying flow field is transonic and highly unsteady. Numerical prediction of unsteady flow phenomena considerably increases the computational cost and requires accurate modelling of turbulent dissipation effects.

It is perhaps unsurprising that, even with rapid advances in computational capabilities in recent years, first-time prediction of capacity to high accuracy is extremely challenging. The purpose of ultra-high accuracy experiments is therefore twofold. First, such experiments can be used for direct capacity evaluation of a particular vane, for engine optimisation during a development programme. Second, building up a bank of ultra-high accuracy experimental measurements provides a reference source for continual development and calibration of numerical capacity prediction processes (both the generation of input geometry, and the CFD solution method).

A minimum requirement for ultra-high accuracy experimental evaluation of vane capacity is a fully annular facility with real engine NGVs, operated at appropriate non-dimensional conditions of Mach and Reynolds numbers. For this reason, capacity measurement has generally been the domain of the OEM due to the prohibitive expense of high-TRL (technology readiness level) facility operation. Much of the effort on the part of the OEM has been aimed at direct validation of capacity for engine design optimisation. Experiments to understand particular sensitivities (e.g. film cooling configuration, trailing edge coolant ejection, coolant-to-mainstream pressure ratio, platform gaps and leakages, etc.) have therefore been rather limited, as have efforts to minimise uncertainty—by whatever means—in the experimental method. Indeed, other than two early papers (referenced below) the only sustained effort towards low-uncertainty capacity measurement and understanding is from the group involved in this paper.

In 1984, Fielding[2] examined the relationship between downstream energy loss coefficients and

boundary layer characteristics at the trailing edge, and defined a parameter which he called *restriction factor*, to account for viscous effects in the vane passage. It can be thought of as a fraction of passage area 'lost' due to momentum deficit in the boundary layer regions. Accounting for losses in this way, as opposed to a basic irreversible 1D estimation, was found to give a change in the estimated capacity value for a typical turbine vane of around 2.4%. In 2004, Afanasiev et al.[3] showed computationally that vanes with identical minimum *geometric* area but different loading distributions can have differences between their capacity characteristics of up to 10%. The difference arises due to a shift in position of the controlling minimum area in relation to the passage. Although retrospectively unsurprising, the importance of this result is highlighted by the persistence, even today, of over-simplistic attempts to reconcile capacity differences between different vanes by ultra-high accuracy measurement of geometric throat area. With improved understanding of the aerodynamic sensitivities (to small design features) of typical HP NGVs, it rapidly becomes apparent that such attempts are unlikely to be successful. Even defining a geometric throat for a highly 3D modern part presents its own challenges.

So far as the published work from the current group is concerned, in 2010, Povey[4] presented an analytical model for estimating the impact of film cooling on capacity based on fundamental cooling performance parameters. This work can be thought of as an extension of Fielding[2] to include film cooling. A control volume mixing approach was employed, in which, importantly, the free-stream static pressure was allowed to vary in the flow direction, in line with the models of, for example, Kollen and Koschel.[5] The conclusions from this work are summarised later in this paper.

In a related 2011 paper, Povey et al.[6] described for the first time a novel semi-transient experimental technique for NGV capacity measurement. By careful experimental design, the semi-transient technique offered a shorter test duration (approximately 60 s), reduced operating cost, and improved precision and bias uncertainty relative to the conventional (continuously running) industrial method. A fully annular cascade of engine components was operated at non-dimensionally engine representative conditions of Mach number, Reynolds number and coolant-to-mainstream pressure ratio. Precision and bias uncertainties in vane capacity of $\pm 0.028\%$ and $\pm 0.546\%$, respectively, were achieved (to 95% confidence). Of the $\pm 0.546\%$, $\pm 0.500\%$ was inherited from the primary mass flow metering nozzle. This is the bias error in the nozzle calibration, traceable to an international standard. The method was designed to minimise the small additional uncertainty ($+0.046\%$) arising from the experimental measurement process. In the same paper, the impact of the definition of the vane exit static pressure on the capacity characteristic was considered. Simplified 1D, 2D (radial pressure profile) and 3D (radial and circumferential pressure profiles) analytical models were compared to experimental data for a modern HP NGV. A poor match between the *shape* of the experimental characteristic and any of the analytical models demonstrated the complexity of the flow environment. This highlights the pitfalls of applying simplified logic based on 1D isentropic equations (e.g. the simplistic—in this context—concept of a *throat*). The disagreement (between models and experiment) in both shape and absolute level were taken to be partly due to total pressure loss, but primarily due to the difficulty in establishing a pressure measurement at a point of well-defined area. This latter point is interesting: the most robust measurement location for static pressure (see later discussion) is on the vane downstream platform, but this is reasonably far from the controlling region where the area is smallest (however defined). In contrast, at locations of well-defined area it would be hard to measure pressure boundary conditions adequately with any practical instrumentation (indeed, an *integration* across a plane would be required to measure capacity directly).

In 2012, Hambidge and Povey[7] investigated the impact of a typical film cooling arrangement on HP NGV capacity using a 2D numerical method. This is can be thought of as a computational extension of Povey.[4] For a typical vane operating at unit Mach number, introducing film cooling was found to cause a 0.125% fall in capacity. This was compared against the analytical model of Povey,[4] which predicted a corresponding capacity drop of 0.144%. It was demonstrated that the effects of multiple rows blowing simultaneously can be closely approximated by superposition of each row blowing in isolation. The errors incurred in making this simplification were of order 0.01% of overall vane capacity. It was therefore concluded that the impact of film cooling typically depends primarily on coolant mass flow, and to a much lesser degree on the actual film cooling arrangement. The impact can likely be adequately accounted for via analytical methods, correlations based on single-row experiments or simulations, or simple 2D CFD.

Since 2011, the semi-transient technique reported by Povey et al.[6] has been used to support a number of engine programmes, and has been the subject of continuous validation and improvement over a series of more than 10 major test campaigns. This facility (Povey et al.[6]) is referred to as the *original facility*. The semi-transient method has been demonstrated to have equivalent or higher accuracy (made possible by more accurate control of experimental conditions) than continuous running facilities, but offers very significant savings in both time and cost. In 2014, the Oxford capacity facility was upgraded to become part of the Oxford Engine Component Aerothermal (ECAT) test bed, offering significantly enhanced capability including metal effectiveness

and downstream traverse measurements.[8] This facility (Kirollos et al.[8]) is referred to as the *current facility*.

With the maturation of the test technique, and the desire for ever-greater accuracy in capacity evaluation, there has been a drive to further optimise the accuracy of the technique, to allow for ultra-low uncertainty (primarily bias error) measurements. This has become particularly relevant in recent years, as the calibration uncertainty of primary nozzles can now be as low as ±0.250% (half the typical lowest uncertainty possible when the original facility was built). This paper concerns key improvements to the test methodology which lower the overall uncertainty of the measurement technique. In particular, improvements in experimental hardware and instrumentation, test methodology, and processing. The impact of each improvement on the additional bias uncertainty in the final capacity measurement is evaluated, and the precision error in the mean is evaluated from a series of repeat experiments. The improvements to the test technique and working section are:

1. Modular construction of the working section and NGV cascade module. This offers improved test efficiency, rapid interchanging of NGV modules, and reduced bias error between repeat test campaigns using the same cascade.
2. Reduced uncertainty in cascade inlet conditions of stagnation pressure and temperature due to increased quantity of measurements.
3. Reduced uncertainty in cascade exit conditions of static pressure distribution due to increased quantity and density of measurements.
4. Independently metered coolant supply streams, allowing for improved benchmarking of coolant mass flow rates. This allows studies of, for example, sensitivity of capacity to coolant-to-mainstream pressure ratio and mass flow rate. Because the bias uncertainty in the measurement of coolant stream mass flow rates is uncorrelated to that in the mainstream mass flow rate, independent metering offers a small reduction in overall bias error.

Each of these aspects—and the associated impacts on the measurement process uncertainty—will be discussed and analysed in turn. The overall uncertainty in the measurement of vane capacity is discussed in detail and compared between the current[8] and original[6] facilities. A *proposed upgraded facility* is also considered. This would take advantage of improvements in nozzle calibration to reduce the primary nozzle calibration uncertainty from ±0.500% to ±0.250%. This improvement derives from advances in the accuracy of the techniques employed at the primary calibration station (a gravimetric method is used, and instrumentation has improved in recent years.). The facility would then represent state-of-the-art in every respect, and defines a practical limit for uncertainty in such facilities. The paper concludes with a detailed comparison of bias, precision, and overall uncertainty in vane capacity measurement in each of the original, current, and proposed upgraded facilities.

Achieving ultra-low uncertainty in the measurement technique makes it possible to examine and understand the impact on capacity of secondary influences such as film cooling, trailing edge coolant ejection, surface deterioration, vane inlet conditions of swirl and turbulence, and small geometry features such as discontinuities and irregularities from casting and installation.

Experimental facility

The Oxford ECAT facility is an engine-scale, semi-transient blowdown facility. Air is stored at 400 psi (27.6 bar) in 60 m^3 tanks, allowing tests at very high energy density for sustained periods (up to 100 s) at relatively low installed plant cost. During a test, the air is discharged through an annular cascade of HP NGVs. The facility is typically used to investigate engine parts from current civil engines. Thus the parts typically have heavy film cooling and coolant ejection from a trailing edge slot. A high degree of non-dimensional similarity (to engine operating conditions) is achieved in the facility, with Mach number, Reynolds number and coolant-to-mainstream pressure ratio being matched. A schematic diagram of the test bed layout is shown in Figure 1.

The facility can be built with a variety of working sections dedicated to metal effectiveness, downstream loss, capacity measurements, or any combination of these. The facility has the capability to replicate both rich-burn and lean-burn inlet conditions, including swirl and temperature profiles. Further details of the ECAT facility capabilities for aerodynamic and heat transfer measurements can be found in Kirollos et al.[8] The facility has a unique modular construction which allows different vane modules to be rapidly interchanged without compromising the sealing integrity. The vane module is built as a stand-alone assembly. Because of the variability in engine parts, wet-seals are required to make up gaps at the platform interfaces. Module components are held in place by a steel fixture during the sealing process to ensure precise alignment of the built module, with gaps to accommodate sealant and allow for slight part variability. Cassettes around the annulus allow easy insertion and reconfiguration of upstream instrumentation. The construction, sealing and testing of the vane module is described in the following section.

The ECAT facility can operate in two modes: *blowdown mode* or *regulated mode*. Blowdown mode is used for measuring capacity over a wide range of operating conditions. In this mode, total temperature and pressure at the cascade inlet steadily drop over

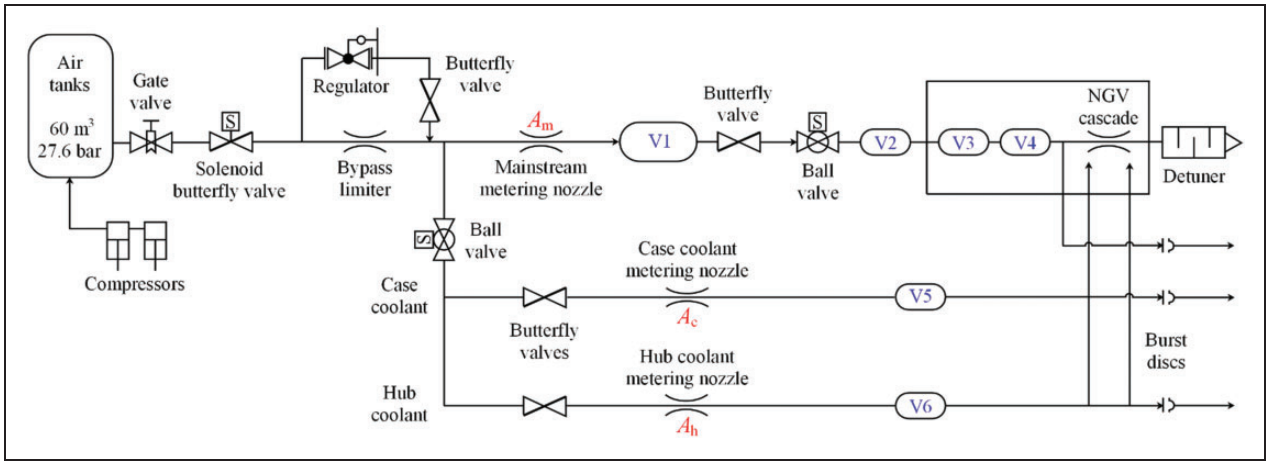

Figure 1. Schematic diagram of the capacity test core installed in the Oxford ECAT test bed.

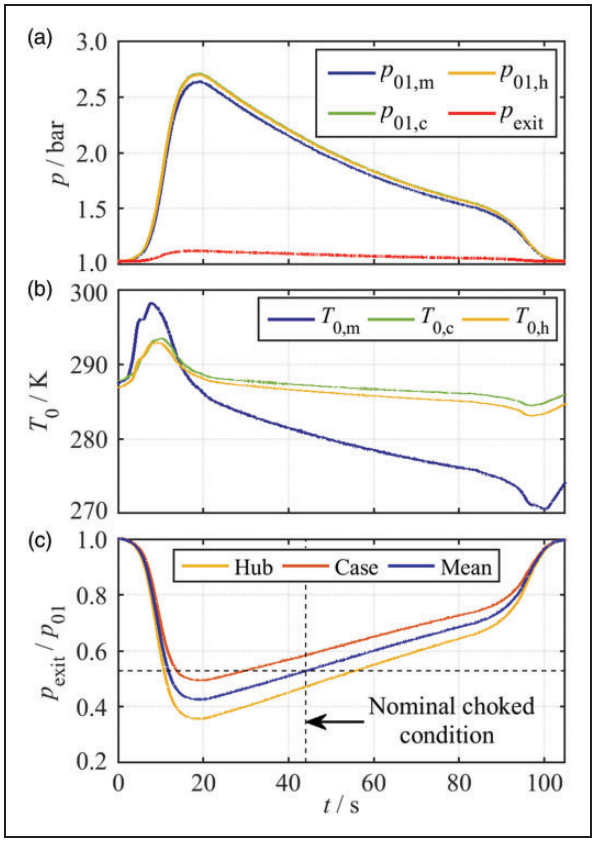

Figure 2. Pressure (a), temperature (b) and vane pressure ratio (c) characteristics during a typical blowdown run.

the course of a test as the supply air tanks are slowly depleted. Pressure and temperature characteristics from a typical run (blowdown mode) are shown in Figure 2. The blue line represents the inlet total pressure of the mainstream feed. After an initial transient of approximately 15 s, the pressure settles to a stable characteristic (between 20 and 85 s) during which time the capacity measurement is performed. The yellow and green lines (which overlay almost exactly) represent coolant total pressures measured in the hub and case feed plena respectively. The ratio of hub and case coolant-to-mainstream mass flow rates are carefully set to match the coolant-to-mainstream total pressure ratios to the engine design condition during the period of stable operation.

During the period of quasi-steady operation, the vane pressure ratio (and Mach number) passes slowly down a characteristic, traversing a range through the design value. The vane pressure ratio trend from a typical run is shown in Figure 2(c). The mean vane pressure ratio varies between $0.43 < p_{exit}/p_{01} < 0.72$, corresponding to a Mach number range $0.70 < M < 1.17$. Thus, a full characteristic can (in principle) be determined from a single test. There are two advantages of operating in this mode. First, a full capacity characteristic, $\Gamma(p_{exit}/p_{01})$, can be determined from a single run of the facility. Second, the facility is naturally quasi-steady, eliminating the need to stabilise an operating point (e.g. stable compressor conditions) as would be necessary in a traditional continuous measurement approach.

Regulated mode is used for measuring capacity at a fixed condition and for cross-checks against the semi-transient blowdown measurement technique, as well as performing traverse measurements of the flow field downstream of the NGV cascade at steady-state condition. An inline high-flow pressure regulator is installed in the upstream pipework (with bypass loop, see Figure 1), allowing the cascade inlet conditions to be held at steady-state for a period of up to 60 s.

Vane module construction and sealing

The vane module has a clamshell-style design, shown schematically in Figure 3. The four principal components—(1) to (4)—and the five potential leak paths—A to E—are marked in the figure.

To ensure precise alignment of the components, the vane pairs (typically 20) are located with dowels on

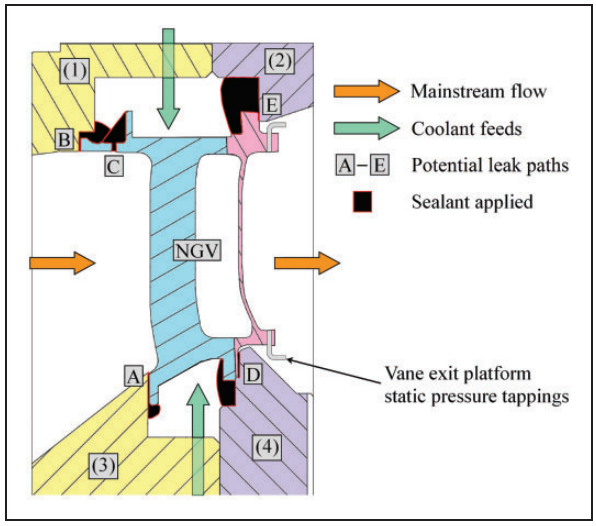

Figure 3. De-featured section schematic of the vane module assembly showing potential leak paths and associated wet seal locations. The main components are: (1) case front support ring; (2) case rear mount ring; (3) hub front support ring; (4) hub rear mount plate.

the hub rear mounting plate, and sealed with a wet seal (aerospace grade silicone sealant) to avoid leaks. The location of the seal is marked 'D' in the figure. At the same stage, seal E is made with the case rear mount ring, and the components are bolted to the hub rear mount plate. During this process, the case rear mount ring and hub rear mount plate are held in place with respect to each other using a ground steel fixture. This ensures precise concentricity and axial alignment while the seals are wet.

Upstream hub and case support rings are then fitted over the vane front platforms and bolted to the hub rear mount plate and case rear mount ring respectively. The components are doweled to ensure precise alignment, and clearance spaces are allowed at locations A and B, designed to account for variability in the cast engine components, and sealed with wet sealant during assembly. The upstream hub and case support rings also form part of the annulus line of the working section.

After assembly, the module dimensions are carefully checked. All mating surfaces are machined (as opposed to cast) to achieve high build accuracy. The vane module seals to the working section components using O-rings, allowing rapid interchange of vane modules without disturbing the wet seals. The ground steel fixture remains attached to the components during assembly (and bolting) into the working section, after which it is removed. This ensures that the components remain in a fixed position during assembly, and therefore that no stress can be imparted to the wet seals during the process.

There are two further advantages of the clam-shell module design. First, a vane module can be stored separate from the main working section, and in a particular build configuration, and re-tested at a future date. For studies of vane capacity targeting deltas of order 0.1%, this capability is extremely useful as it removes an additional source of uncertainty between repeat tests (variability in the precise installation of the vanes in the module). Second, the removable vane module opens the way for back-to-back testing of NGVs with small geometric changes introduced sequentially to the module—e.g. studies of damage to leading or trailing edges, which can be simulated by sequential machining of the components. The ability to make such changes without dismantling the vane module or disturbing the wet seals makes it possible to detect very small shifts in vane capacity.

It is important to distinguish between primary and secondary leak paths through the vane module. Primary leak paths (D and E in Figure 3) allow air from the coolant cavities to bypass the vane and flow directly into the downstream system. Incomplete sealing at these locations would cause error in the capacity measurement and must be avoided. Secondary leak paths (A, B and C in Figure 3) allow coolant flow into the mainstream channel upstream of the cascade. This would affect the cascade inlet flow condition, and consequently have a secondary influence on capacity. Table 1 summarises the leak paths.

Prior to an experimental test campaign, a series of tests are conducted to check the integrity of the working section seals. This is required to ensure that leaks do not influence the measured capacity result. The process is now described.

The tests involve feeding only the two coolant streams (not the mainstream feed) and accurately measuring the total coolant flow capacity characteristic (up to approximately ten times a typical design coolant-to-mainstream pressure ratio) in the *ex-situ* environment (no aerodynamic field due to the main flow). The measured capacity characteristic is then compared to a second set of measurements performed on a statistically large sample of vanes (10–20 vane pairs from the cascade) in individual bench-test experiments. In the bench-test experiment, coolant is supplied from both hub and case feeds (pressure balanced), and coolant flow capacity is measured at a number of coolant-to-downstream pressure ratios. Agreement between the two coolant capacity data (good overlap of the uncertainty bounds) is taken as indication of good build integrity. These tests are referred to as *dynamic leak tests*. As the coolant capacity is only a small fraction of the overall capacity (typically $< 10\%$), and because high accuracy can be achieved in the dynamic leak tests, they provide an accurate method of diagnosing unintended leak paths.

Figure 4(a) shows typical coolant capacity characteristics (solid lines) from four separate sets of tests of the same parts, taken at intervals during a 12-month period. Between each set of tests, the vane module was removed from the facility working section and reinstalled. In this particular example, an external machining operation was performed on the vane ring between each test, to study the effect of trailing edge cut-back on

Table 1. Summary of working section leak paths.

Leak path	Primary/secondary	Description
A	Secondary	Hub coolant cavity into mainstream through annular gap between vane hub front platform and hub support ring
B	Secondary	Case coolant cavity into mainstream through annular gap between vane case front platform and case support ring
C	Secondary	Case coolant cavity into mainstream through vane case platform cooling holes
D	Primary	Hub coolant cavity into downstream through annular gap between vane hub rear platform and hub mounting plate
E	Primary	Case coolant cavity into downstream through annular gap between vane case rear platform and case mounting plate

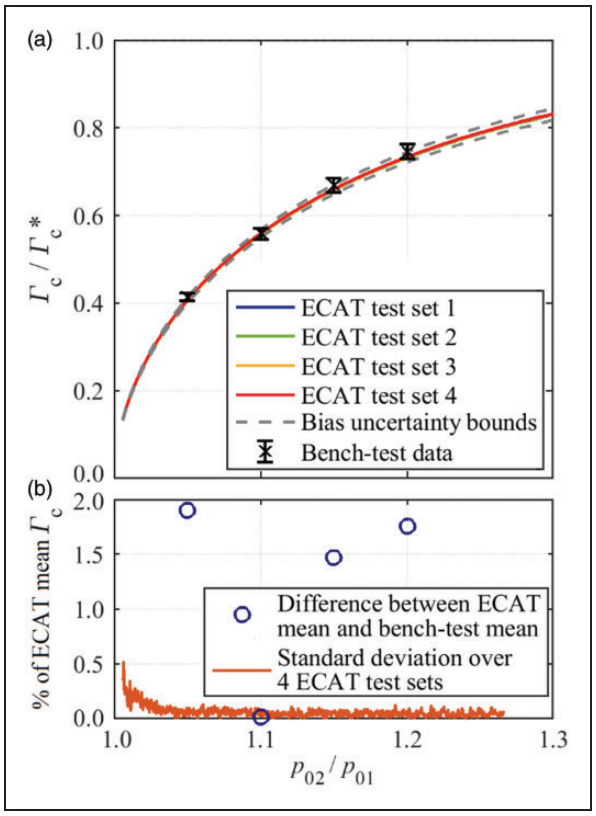

Figure 4. (a) Coolant capacity characteristics measured in dynamic leak tests in four ECAT test campaigns over a 12-month period, compared against bench-test data; (b) percentage standard deviation between different ECAT test sets, and percentage difference between ECAT and bench-test data.

capacity. This operation was external to the trailing edge slot, and not expected to affect the coolant capacity in the absence of mainstream flow.

A typical test set is composed of six runs, allowing both the mean characteristic and the precision error in the mean to be calculated. We see that the four data sets overlay so closely that the individual lines are indistinguishable. The average standard deviations *within* each of the four data sets, averaged over the range $1.01 < p_{02}/p_{01} < 1.27$, were 0.11%, 0.10%, 0.11% and 0.09%. These very low values confirm the high degree of stability and repeatability in the measurements.

The standard deviation *between* the four data sets is shown in Figure 4(b) (orange line). Over the pressure ratio range $1.05 < p_{02}/p_{01} < 1.27$, the standard deviation was 0.05%. The standard deviation between the four trends is therefore lower than that between individual runs comprising a trend. This confirms the extremely high repeatability of the coolant capacity measurements over four separate builds of the facility in a 12-month period. It is concluded that no unintended leaks were introduced during this time. The bias error in coolant capacity measurements in the ECAT facility was calculated as ±1.62% to 95% confidence (indicated by dotted lines on the plot). This bias uncertainty was calculated following the method presented in the later section on uncertainty analysis. Inputs included the measured coolant cavity total pressures and temperatures, coolant stream mass flow rates and vane external static pressure in the *ex-situ* (no external aerodynamic field) situation.

The black crosses in Figure 4(a) represent the average from bench test capacity measurements (i.e. individual vane pairs measured in a separate facility) of 14 vanes, conducted at four discrete pressure ratios. The error bars on the bench-test data points (Figure 4(a)) represent two standard deviations for the distribution of coolant capacity values for the set of 14 vane pairs tested. The average (across four operating conditions) standard deviation was 4.58% of the mean capacity value, corresponding to a standard error in the mean (of 14 vanes) of ±2.45% to 95% confidence. The bias uncertainty was evaluated (in separate uncertainty analysis) as ±0.40% (95% confidence). Mass flow rate measurements in the bench test were made using a sonic Venturi nozzle calibrated by CEESI, with calibration traceable to a national standard. The difference between the mean ECAT data (across four test sets) and the bench-test data, taken at the four discrete pressure ratios is marked in Figure 4(b) (blue circles). The average across these four points was 1.28%. The two data have overlapping uncertainty bands indicating this is a likely result for a build with no leaks.

Coolant capacity data (dynamic leak tests) are typically collected over a range of coolant-to-mainstream pressure ratio $1.0 < p_{02}/p_{01} < 1.3$, where $p_{01} \approx p_{exit}$. In

this *ex-situ* situation (no mainstream flow), the maximum pressure difference across the wet seals is approximately $p_{02} - p_{exit} = p_{02} - p_{atm} = 0.3$ bar. This is considerably lower than at typical *in-situ* operating conditions, where the pressure difference $p_{02} - p_{exit}$ can be as large as 1.5 bar (see Figure 2), being greatest across the wet seals of *primary* leak paths (D and E in Figure 3). Thus the coolant capacity check poses no additional risk to the seals over that experienced in a typical run. It is considered good practice to repeat the check at the end of a test campaign, to confirm there has been no damage to any seals.

The coolant capacity characteristic in Figure 4(a) can be extrapolated to a choked condition by fitting an isentropic capacity curve. This allows the ratio of the estimated choked coolant capacity, Γ_c^*, to the choked vane capacity, Γ_{vane}^*, to be estimated. This gives $\Gamma_c^*/\Gamma_{vane}^* = 0.152$. In the worst-case scenario in which a leak in an incompletely sealed vane module was entirely a primary flow leak, a leak with a capacity equivalent to the difference between the mean of the four ECAT datasets and the bench-test data (1.29% of Γ_c^*) would equate to 0.20% of Γ_{vane}^*. The dynamic leak check is a robust way of reducing the risk of leaks affecting NGV capacity measurement.

Mass flow rate measurement

Flow into the facility is split into three separate streams: mainstream flow, and hub and case coolant supply flows. Each stream is controlled and metered by an independent choked nozzle. The mainstream flow is fed by a 3″ diameter sonic Venturi nozzle (labelled A2 in Figure 1). The nozzle was calibrated to a National Institute of Standards and Technology (NIST) traceable standard at Colorado Engineering Experiment Station Inc. (CEESI) and installed according to ISO 9300.[9] The bias uncertainty associated with the measurement is ±0.500% (to 95% confidence).

The NGV coolant feeds are supplied with air via separate hub and case supply streams. The coolant stream mass flows are controlled and metered using sonic Venturi nozzles. These are labelled A3 and A4 in Figure 1. The air feeds are drawn off downstream of the regulator and bypass line, but upstream of the main nozzle. This ensures (instantaneously) essentially identical feed pressure to all three nozzles (mainstream, hub and case coolant) giving ratiometric mass flow rates, even during blowdown mode operation in which the facility passes down a characteristic. The coolant metering nozzles are interchangeable, allowing precise adjustment of coolant-to-mainstream mass flow rates and pressure ratios at the NGV. The overall NGV capacity accounts for both mainstream and coolant flows. This is discussed in a later section.

Mass flow rate unsteady correction

During a blowdown test, the pressure and temperature in the main tank decay as the tank is emptied, following an approximately isentropic expansion. Likewise, the pipework system and working section pass down a pressure characteristic as seen in Figure 2. During this process, the mass stored in each of the pipework volumes reduces over time. This effect causes a small discrepancy between the mass flow rates passing through the metering nozzles, and those delivered at the test vane. The rate at which the mass stored in the *intermediate plena* (those volumes located between the metering nozzles and points of delivery to the vane) is depleted must be accounted for. This correction is considered now.

The intermediate plena are indicated schematically in Figure 1, and labelled V1–V6. V1–V4 are intermediate plena on the mainstream flow path. V5 and V6 are the intermediate plena on the case and hub coolant flow paths, respectively. Assuming ideal gas behaviour, the rate of change of stored mass in an individual plenum is given by

$$\dot{m} = \frac{\mathrm{d}}{\mathrm{d}t}\left(\frac{pV}{RT}\right) = \frac{V}{RT}\left(\frac{\mathrm{d}p}{\mathrm{d}t} - \frac{p}{T}\frac{\mathrm{d}T}{\mathrm{d}t}\right) \tag{2}$$

The total *mainstream* unsteady correction mass flow is therefore given by the sum

$$\dot{m}''_m = \sum_{i=1}^{4} \dot{m}_i = \sum_{i=1}^{4} \frac{V_i}{RT_i}\left(\frac{\mathrm{d}p_i}{\mathrm{d}t} - \frac{p_i}{T_i}\frac{\mathrm{d}T_i}{\mathrm{d}t}\right) \tag{3}$$

Corrections for the coolant stream plena, V5 and V6, follow the same form.

Overall mass flow rate for a typical blowdown run (same run as Figure 2) is plotted in Figure 5(a). The mass flow rate characteristics are truncated at the beginning and end of the test when the pressure ratio across the metering nozzle fails to reach the critical choked condition. Outside of this range, the nozzle is out of its calibration range, and mass flow rate is not computed. During the pressurisation of the working section, the total mass flow rate through the vane lags behind the combined mass flow rate measured through the three feed nozzles. This effect results from mass accumulation in the intermediate plena. Positive mass accumulation is associated with the increase in pressure during pressurisation of the facility. For completeness, it is noted that the increase in pressure is accompanied by an increase in temperature (below the isentropic compression rate, due to heat transfer), which reduces the accumulation rate due to a density decrease with temperature.

The overall mass accumulation rate is plotted in Figure 5(b). The rate of mass accumulation has a maximum value of around 2 kg s^{-1} (at approximately $t = 10$ s) during the initial pressurisation of the facility

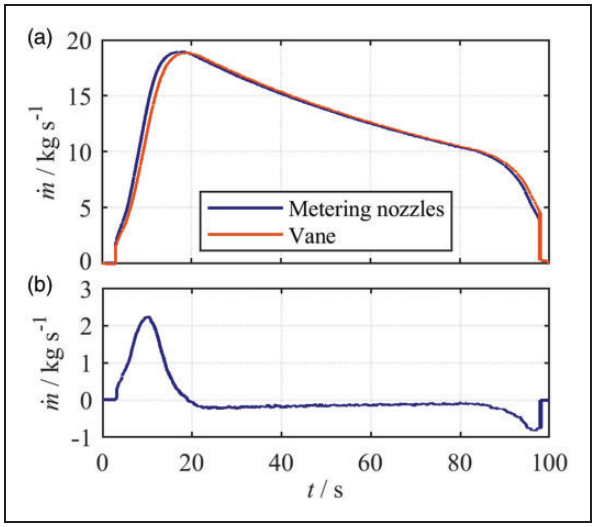

Figure 5. (a) Overall mass flow rate characteristics for a typical blowdown test (rescaled to an arbitrary maximum of 19.0 kg s^{-1}); (b) overall mass accumulation rate in intermediate plena.

working section. During the period of quasi-steady operation (20–80 s), the quantity of mass stored in the plena reduces as the pressure falls. The maximum depletion rate (at $t \approx 20$ s) is 0.26 kg s^{-1} and steadily decays over the course of the test period. The vane mass flow rate at the same time is 19.0 kg s^{-1}, giving a maximum correction during the quasi-steady period of approximately 1.37%.

As will be discussed in detail later, the bias uncertainty in the correction mass flow rate is approximately ±13.1% (to 95% confidence), leading to an increase in the bias uncertainty in the vane mass flow rate measurement (over that at the main metering nozzle) of approximately 0.015%. Performing the unsteady correction therefore contributes only a small amount to the overall uncertainty.

Inlet total pressure and temperature measurement

Measurements of total pressure and temperature at vane inlet are performed with cassette-mounted probes just upstream of the vane module in the mainstream flow, and in the coolant supply plena for the hub and case coolant flows. Measurement locations are shown in the section diagram of Figure 6.

Inlet total pressure and temperature to the cascade were each measured at 32 locations, each using four probes at separate circumferential locations. On each probe, the measurement locations were distributed evenly across the span. The measurement plane was located four axial chords upstream of the cascade leading edge. The cassettes are interchangeable and reconfigurable, allowing optimisation of the instrumentation according to the test requirements. There are four cassette locations around the annulus, and each cassette can accommodate up to six probes.

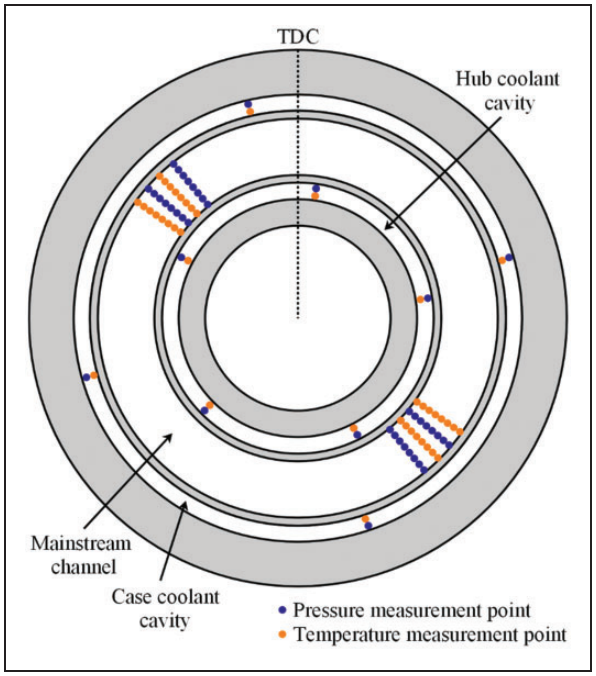

Figure 6. Locations of inlet condition measurements for mainstream and coolant flows, viewed from downstream.

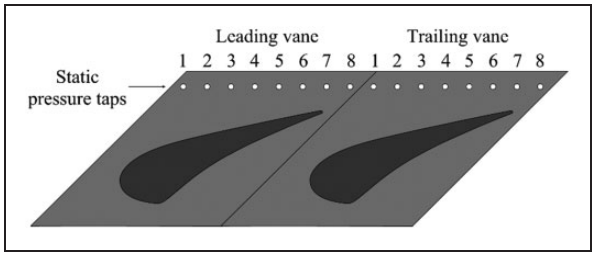

Figure 7. Simplified view of a vane pair exit platform instrumented with eight static pressure tappings per passage.

Hub and case coolant inlet total pressure and temperature were each measured at five and four evenly spaced locations around the annulus, respectively. These measurement points are located in the hub and case coolant cavities of the vane module, which feed coolant flow into the vane internal cooling systems.

Exit static pressure measurement

Static pressure at vane exit is measured on the hub and case downstream platforms of three instrumented vane pairs (six vanes from a typical total of 40). Figure 7 shows a simplified diagram of the locations of static pressure tappings on a typical instrumented vane pair platform. The location of a tapping on the vane platforms is illustrated in Figure 3. The three instrumented vane pairs are spaced 120° apart around the annulus. A typical test campaign uses eight tappings per vane pitch at hub and case. For a total of 12 instrumented platforms (six at the hub and

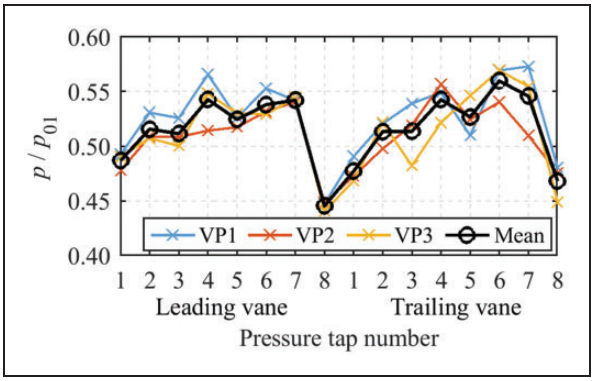

Figure 8. Example of a typical measured circumferential static pressure profile on three instrumented vane pair platforms. The x-axis represents the tapping locations shown in Figure 7.

six at the case), this gives 96 tappings. The significance of the number of tappings to the bias uncertainty in the vane exit static pressure condition is discussed later in this paper.

Example circumferential static pressure profiles measured on three vane pair platforms from a typical experiment are plotted in Figure 8 for an arbitrary mean operating pressure ratio of 0.46 (note the measured static pressures are offset from the nominal mean value due to the radial pressure gradient). The three instrumented vane pairs are distinguished as VP1, VP2 and VP3. The three vane pairs give very similar trends, with average standard deviation between measurements of 3.5%. Small differences arise due to repeatability in the cast part geometry. Run-to-run repeatability was excellent, with an average standard deviation of 0.10% between data (at the same measurement location and *mean* pressure ratio) from 17 repeat tests. In a later section, the sensitivity of vane capacity measurement to tapping number, axial location, and positional accuracy is analysed.

Capacity definition for fully cooled NGVS

Consideration is now given to the definition of capacity in a system with several streams at different conditions of inlet total pressure and temperature. This is relevant to an HP NGV because a typical vane has a mainstream flow, coolant flow ejected from film cooling holes (often distributed over the vane surface) and coolant ejection from the trailing edge.

A schematic representation of a typical HP vane cooling system is presented in Figure 9. The flow system can be characterised by a mainstream flow (subscripted 1), a film cooling system (subscripted 2), simplified to a single stream for the purpose of this analysis, and a trailing edge coolant outlet (subscripted 3). At engine conditions the two coolant flows generally enter at significantly lower total temperature than the mainstream, and marginally higher total pressure. Comparisons between systems therefore depend on the particular definition of capacity used. In this system, film cooling flow (2) enters the

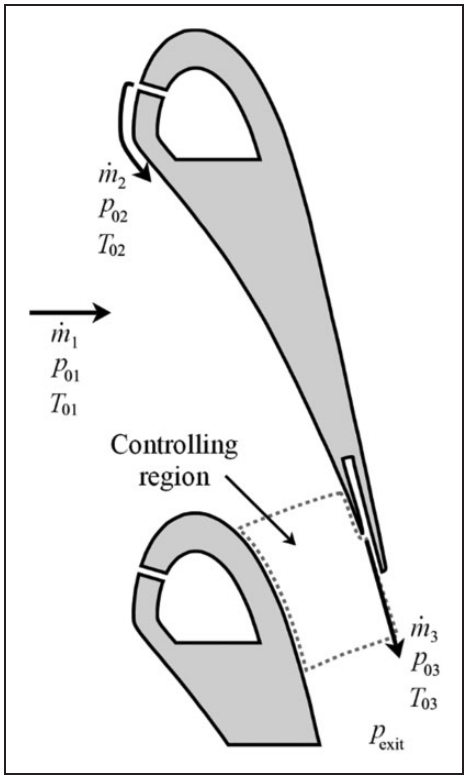

Figure 9. Schematic of a typical HP vane cooling system showing mainstream flow (1), film cooling flow (2), and trailing edge coolant flow (3).

mainstream in a low Mach number region and partially mixes before passing through the *controlling region* (this terminology is discussed below) of the passage. Trailing edge coolant (3) enters the domain within the (loosely defined) controlling region.

In the description above, the traditional terminology of a *vane throat* was avoided, as it gives rise to misleading notions which are only applicable to 1D systems. The minimum *geometric* passage area can be determined by reference to CAD drawings of the part or by using techniques such as structured light scanning to directly measure the part geometry. The complex 3D geometry of some parts further complicates even the practical definition of a minimum physical area. Should the definition be restricted to a flat plane or should the area be defined as that integrated across projections normal to the local streamlines? However, this alone gives poor insight into the vane capacity.

It is well established that NGVs with the same geometric minimum area can have capacity characteristics that differ by 10% or more.[3] Indeed, a typical HP vane has a large region of fairly complex flow in the transonic Mach number range. At the point of minimal physical area (defined either by a plane or a more complex surface), the flow is generally found to be either sub-or super-critical over most of this 'throat', often by a significant margin. Indeed, for a vane operating at a nominally choked (based on 1D assumptions) pressure ratio, the sonic surface can pass through the minimum physical area with quite a

high angle of intersection (i.e. the sonic surface and the surface of minimum physical area are poorly aligned). In some cases, the sonic surface is not bounded by the vane passage, but extends out into the wake region downstream. This rather fundamental observation brings into question the usefulness of concepts of minimum geometric area.

The question therefore arises as to the most appropriate way to define vane capacity in a multi-stream system. The simplest definition might be to base the capacity definition on the overall mass flow, and the mainstream total temperature and pressure:

$$\Gamma_{\text{vane}} = \frac{\dot{m}_{\text{total}}\sqrt{T_{01}}}{p_{01}} \tag{4}$$

One objective in evaluating the suitability of a capacity definition, however, might be that it be as independent as possible of the individual stream flow properties (in the simplest case this means the inlet total pressure and temperature for each stream)—i.e. the capacity should change as little as possible when the individual stream properties change. Three simplified representations of the system in Figure 9 are now considered.

Model 1

In the first model, three initially independent streams fully mix at low Mach number before being accelerated to uniform exit conditions at a single controlling area. This model is referred to as the *fully mixed, multi-stream, single controlling area model*. It is illustrated schematically in Figure 10.

In this system, the mass flow rate through the controlling area depends only on the flow conditions of the fully mixed flow stream and the downstream static pressure (p_{exit}). The average total temperature (assuming constant c_p) at this location is

$$\overline{T_0} = \frac{\dot{m}_1 T_{01} + \dot{m}_2 T_{02} + \dot{m}_3 T_{03}}{\dot{m}_{\text{total}}} \tag{5}$$

where the total mass flow rate, $\dot{m}_{\text{total}}$, is the sum of the three individual stream mass flow rates. Total pressure averaging should properly be done using a control volume mixing model, but this strays towards analytical prediction of capacity which is inherently problematic for reasons discussed (strong dependence on the aerodynamic state of the controlling region). For the purpose of this simple model, and considering that cooling mass flow rates are typically relatively small (up to 10% of the total flow) and with only a small difference in total pressure condition between mainstream and coolant (typically within 3%), it is considered adequate to adopt the following mass-flow averaged definition

$$\overline{p_0} = \frac{\dot{m}_1 p_{01} + \dot{m}_2 p_{02} + \dot{m}_3 p_{03}}{\dot{m}_{\text{total}}} \tag{6}$$

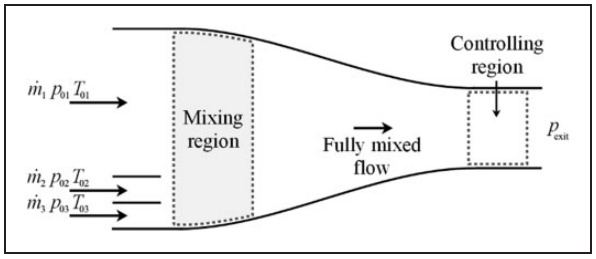

Figure 10. Schematic diagram of the fully mixed, multi-stream, single controlling area model.

This leads directly to the following definition of capacity

$$\Gamma_{\text{vane}} = \frac{\dot{m}_{\text{total}}\sqrt{\overline{T_0}}}{\overline{p_0}} \tag{7}$$

For completeness, it should be noted that a difference in c_p between the streams (e.g. that seen between mainstream and coolant flows in the engine situation) would require equation (5) to be adapted. It may also be necessary to consider the variation in gas properties (γ and R) between the streams.

In systems which can be approximated by the model of Figure 10, the definition in equation (7) should be relatively insensitive to the individual stream properties. Recalling the caveats regarding the evaluation of the average flow properties passing through the controlling area, effects leading to incorrect averaging would cause capacity differences between systems that, in the framework of this model, would be considered nominally identical (same controlling area). That is, whilst definition (7) is to some extent insensitive to individual stream properties, simplifications in the model mean it is not entirely so.

Model 2

In the second model, the streams are considered to be entirely independent of one other. That is, they each have independent controlling areas which do not interact. This model is illustrated in Figure 11. This system is referred to as the *unmixed, multi-stream, multiple controlling area model*, and represents the opposing extreme to Model 1. The capacity of this system is represented by the sum of the three individual stream capacities

$$\begin{aligned}\Gamma_{\text{vane}}\left(\frac{p_{\text{exit}}}{p_{01}}, \frac{p_{\text{exit}}}{p_{02}}, \frac{p_{\text{exit}}}{p_{03}}\right) = {} & \frac{\dot{m}_1\sqrt{T_{01}}}{p_{01}}\left(\frac{p_{\text{exit}}}{p_{01}}\right) \\ & + \frac{\dot{m}_2\sqrt{T_{02}}}{p_{02}}\left(\frac{p_{\text{exit}}}{p_{02}}\right) \\ & + \frac{\dot{m}_3\sqrt{T_{03}}}{p_{03}}\left(\frac{p_{\text{exit}}}{p_{03}}\right)\end{aligned} \tag{8}$$

where the three right hand side terms are functions of the pressure ratios given in parentheses.

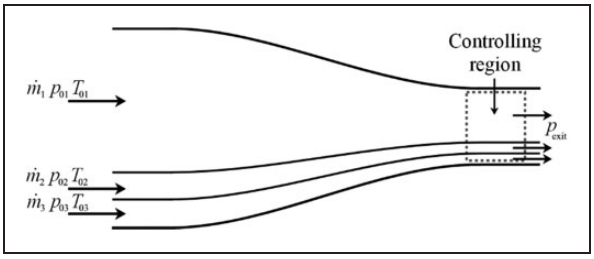

Figure 11. Schematic diagram of the unmixed, multi-stream, multiple controlling area model.

In a typical cooling system (represented in Figure 9), the ratios of the downstream pressure to the coolant stream pressures, p_{exit}/p_{02} and p_{exit}/p_{03}, are generally functions of the vane pressure ratio, p_{exit}/p_{01}, and the coolant-to-mainstream total pressure ratio, p_{02}/p_{01}. The former sets the mainstream aerodynamics and the latter, for a given mainstream flow, sets the coolant flow. Note we make the assumption that the film coolant and trailing edge coolant flows share a common inlet total pressure condition (i.e. $p_{02} = p_{03}$). Equation (8) can therefore be simplified to the following form

$$\Gamma_{vane}\left(\frac{p_{exit}}{p_{01}}, \frac{p_{02}}{p_{01}}\right) = \frac{\dot{m}_1\sqrt{T_{01}}}{p_{01}}\left(\frac{p_{exit}}{p_{01}}, \frac{p_{02}}{p_{01}}\right) + \frac{\dot{m}_2\sqrt{T_{02}}}{p_{02}}\left(\frac{p_{exit}}{p_{01}}, \frac{p_{02}}{p_{01}}\right) + \frac{\dot{m}_3\sqrt{T_{03}}}{p_{03}}\left(\frac{p_{exit}}{p_{01}}, \frac{p_{02}}{p_{01}}\right) \quad (9)$$

Each of the three terms on the right hand side of equation (9) are *surfaces* of capacity. The term on the left-hand side, total capacity, is a surface which is simply the summation of those three terms. Two variables are sufficient to define a position on the surface: the vane pressure ratio (p_{exit}/p_{01}) and the coolant-to-mainstream pressure ratio (p_{02}/p_{01}). A typical capacity surface in (p_{exit}/p_{01}, p_{02}/p_{01})-space is shown in Figure 12. Here the gradient of capacity in the p_{02}/p_{01}-axis has been exaggerated by an order of magnitude from a typical trend to more clearly illustrate the sensitivity in both axes. The negative trend arises because, while the coolant stream capacity terms (second and third terms on the right hand side of equation (9)) increase in magnitude with increasing p_{02}/p_{01}, for many NGVs the effect of mainstream 'displacement' by increased coolant flow is more significant. Surprisingly perhaps, the gradient of Γ_{vane} with p_{02}/p_{01} can be negative even where the coolant flow is a single stream issuing from a trailing edge slot in a cut-back pressure side of the vane.

It is well established that one of the prime sensitivities in setting HP NGV capacity (at the design or manufacture stage) is the interaction of trailing edge coolant flow with the mainstream. The effect is typically greater by at least an order of magnitude than the

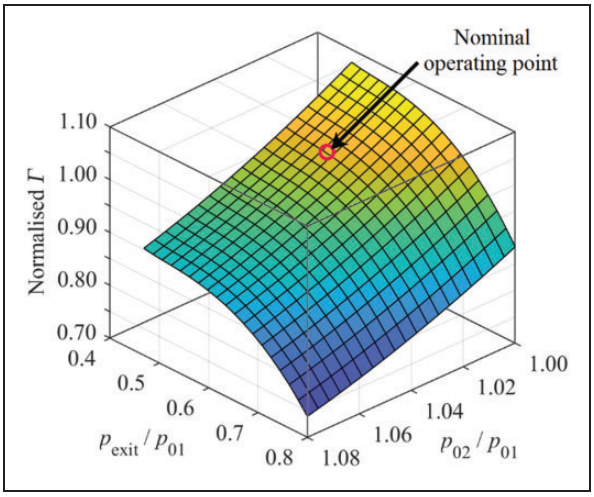

Figure 12. Surface of capacity, as a function of both vane pressure ratio, p_{exit}/p_{01}, and coolant-to-mainstream pressure ratio, p_{02}/p_{01}. The sensitivity to p_{02}/p_{01} has been exaggerated by a factor of 10.

sensitivity to particular film cooling arrangements. The trailing edge sensitivity is a function of both the detailed shape of the part in this region, and coolant-to-mainstream pressure ratio. An advantage of definition (9) is that the sensitivity to p_{02}/p_{01} is inherently built into the definition. This comes at the cost, in this simple formulation, that streams 1 and 2 are considered to be entirely non-interacting. This is a poor representation of most film cooling systems, which are typically fairly well mixed out as they pass through the controlling area.

Model 3

It is possible to construct a hybrid model in which the mainstream and film cooling flows mix fully before passing through a single controlling area, and in which there is an independent controlling area for the trailing edge cooling flow. This model is shown schematically in Figure 13.

A related system to this hybrid model was studied analytically by Povey.[4] Although this study[4] was restricted to only two streams (mainstream and film coolant), a more sophisticated treatment of mixing was developed (by means of a full control-volume approach, accounting for pressure losses in the partially mixed layer and changes in gas properties) allowing for both partial mixing (to a defined film cooling effectiveness) and a particular acceleration (to a defined 'throat' Mach number). In Povey,[4] the difference in capacity between experimental rig and engine conditions for typical boundary conditions was evaluated as a correction parameter. It was concluded[4] that there are unacceptable (of order 1.88%) sensitivities (differences between rig and engine situations) when definition (4) is used. This is because the entire flow is referenced to the mainstream flow properties. The definitions arising from Model 1 are

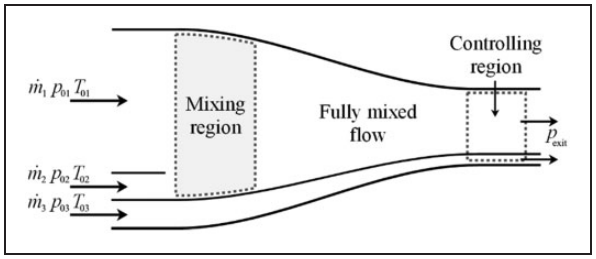

Figure 13. Schematic diagram of a hybrid model involving fully mixed mainstream and film cooling flows (1, 2) and unmixed trailing edge coolant (3).

therefore of little use in translating between systems with different T_{02}/T_{01}. It was also shown[4] that when capacity is based on a fully-mixed-out total pressure and temperature (similar to equation (7)), capacity differences between rig and engine reduce to approximately 0.20%, are proportional to the coolant mass flow (a later study,[7] showed also that this result was surprisingly independent of the specific arrangement of film cooling holes), and are amenable to analytical modelling.[7]

Attention is now turned to the difference between definitions (4), (7) and (9). Here we are concerned with the temperature averaging method alone, and do not consider more sophisticated aspects of the mixing and loss (the latter is treated in Povey[4]). To illustrate the sensitivity to temperature averaging, we simplify typical cold rig (A), warm rig (B), and engine conditions (C) to the values in Table 2.

The current experiments in the ECAT facility are closest to the cold rig situation (A). In all situations, the system has been simplified to a single cooling feed (i.e. $\dot{m}_3 = 0$). This is equivalent to the film cooling and trailing edge cooling flows sharing common inlet conditions p_{02} and T_{02}, with $\dot{m}_2$ representing the total coolant mass flow input to the system.

The sensitivity of capacity—according to these definitions—to variations in the coolant mass flows is also considered. Conditions A′ and A″ are defined to represent variations of −10% and +10% of $\dot{m}_2/\dot{m}_{\text{total}}$ respectively, with respect to the design point condition A. Likewise, pairs of ±10% cooling conditions are defined for situations B and C. The differences between equations (9) and (4) and between equations (9) and (7) are plotted in Figures 14 and 15 respectively, as functions of $\dot{m}_2/\dot{m}_{\text{total}}$ and T_{01}/T_{02}.

Consider first Figure 14 which shows the difference between equations (9) and (4). At cold rig conditions (A), there is no discrepancy between definitions due to temperature averaging alone, as the streams share a common temperature. At warm rig (B) and engine (C) conditions, there are 0.679% and 3.018% differences in capacity (respectively) between these definitions. Perhaps more importantly, consider the sensitivity to coolant mass flow rate variation. Assuming that total mass flow rate, $\dot{m}_{\text{total}}$, remains constant, equation (4) is unaffected by variation in $\dot{m}_2/\dot{m}_{\text{total}}$ (i.e. between

Table 2. Summary of simplified rig and engine conditions.

Situation	p_{02}/p_{01}	$\dot{m}_2/\dot{m}_{\text{total}}$	T_{01}/T_{02}
Cold rig (A)	1.00	0.070	1.0
Warm rig (B)	1.00	0.076	1.2
Engine (C)	1.00	0.100	2.0

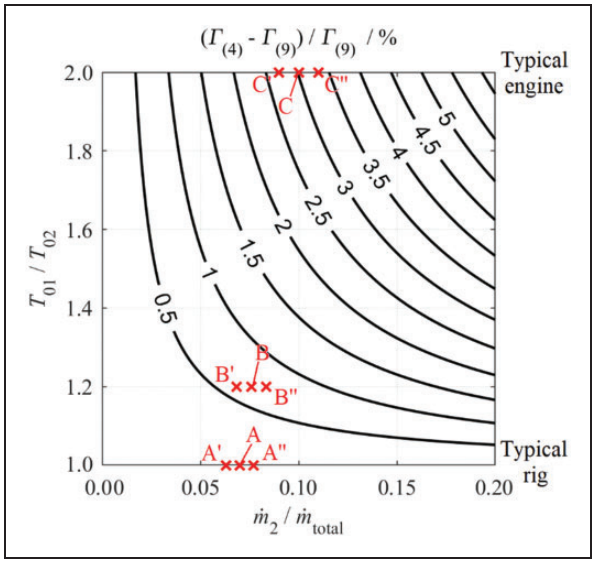

Figure 14. Contours of percentage difference in capacity defined according to equations (4) and (9), as a function of coolant-to-mainstream mass flow ratio and temperature ratio.

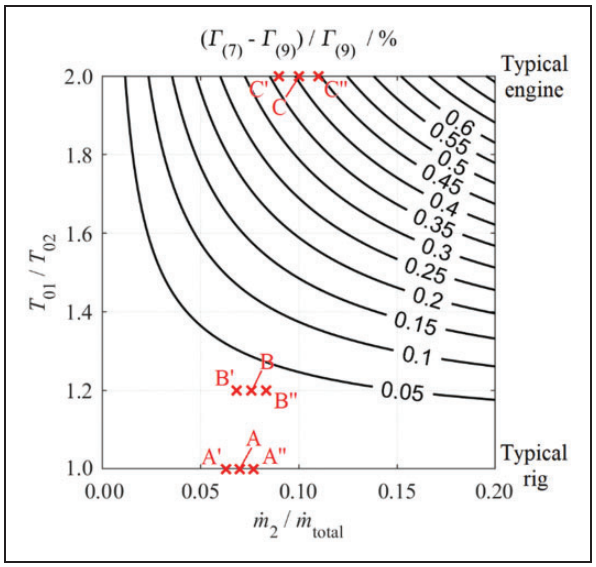

Figure 15. Contours of percentage difference in capacity defined according to equations (7) and (9), as a function of coolant-to-mainstream mass-flow ratio and mainstream-to-coolant temperature ratio.

A′ and A″). Equation (9) changes by 0.133% between B′ and B″, and by 0.603% between C′ and C″. Of course, when performing comparisons across conditions, correct scaling must be performed to ensure

Table 3. Summary of differences in sensitivity of different capacity definitions from Figures 14 and 15.

	$\Gamma_{(4)}$	$\Gamma_{(7)}$	$\Gamma_{(9)}$	Δ between $\Gamma_{(4)}$ and $\Gamma_{(9)}$	Δ between $\Gamma_{(7)}$ and $\Gamma_{(9)}$
$\Delta\Gamma$ at A / %	–	–	–	0.000	0.000
$\Delta\Gamma$ at B / %	–	–	–	0.679	0.028
$\Delta\Gamma$ at C / %	–	–	–	3.018	0.409
$\Delta\Gamma$ from A′ to A″ / %	0.000	0.000	0.000	0.000	0.000
$\Delta\Gamma$ from B′ to B″ / %	0.000	0.128	0.133	0.133	0.005
$\Delta\Gamma$ from C′ to C″ / %	0.000	0.526	0.603	0.603	0.077

these effects (and many others) are accounted for. Nonetheless, this illustrates the points that the exact definition of capacity matters, and that there are relatively high exchange rates between capacity (according to more rational definitions, e.g. equation (9)) and coolant mass flow rate at both warm rig and engine conditions. These results are summarised in Table 3.

Consider now Figure 15, which shows the difference between equations (9) and (7). Again, at cold rig conditions (A) there is no difference in capacity due to temperature averaging alone, as the streams share a common temperature.

At warm rig (B) and engine (C) conditions, there are 0.028% and 0.409% differences in capacity (respectively) between these definitions. These differences are considerably smaller (by an order of magnitude at warm rig conditions) than between equations (9) and (4), showing that the difference between these methods of temperature averaging—i.e. implied by equations (9) and (7)—is relatively subtle.

As coolant mass flow rate is varied at cold rig conditions (A′ to A″), there is no difference in the capacity change between definitions (9) and (7), because the capacity value is insensitive at a temperature ratio of unity. At warm rig conditions (B), ±10% variation in cooling mass flow rate (B′ to B″) gives a capacity change of 0.128% according to definition (7) and 0.133% according to definition (9). The difference in sensitivity between the two definitions is therefore 0.005%. Likewise, at engine conditions (C), the capacity changes with ± 10% variation in cooling flow (C′ to C″) according to definitions (7) and (9) are 0.526% and 0.603%, respectively, giving a difference in sensitivity between the definitions of 0.077%. These differences in sensitivity to cooling mass flow rate are very small indeed.

We conclude that whilst it is helpful (for the purpose of translating between different environments; see also studies[4,7]) for the mass flow rate and inlet temperature of coolant flows to be included in the capacity definition (as in equations (7) and (9), but not in equation (4)), the difference arising from the way in which this is achieved is relatively small. That is, using the square root of the mass-flow-weighted temperature with the total mass flow rate (equation (7)), or using the mass-flow-weighted sum of individual $\sqrt{T_0}$ terms for each stream (equation (9)). As corrections between different conditions (e.g. $\dot{m}_2/\dot{m}_{\text{total}}$ and T_{01}/T_{02}) are reasonably involved, and include many considerations in addition to temperature averaging, equations (7) and (9) appear to share similar usefulness in terms of their robustness (to first order) to changing inlet total conditions of individual streams between systems.

However, the definition in equation (9) has one significant advantage: in the correct experiment, it is possible (by virtue of the form of the equation) to isolate sensitivities to key effects such as trailing edge coolant ejection. That is, where the mass flow rates of the individual streams are independently metered, it becomes possible to identify the change in the mainstream mass flow ($\dot{m}_1$) caused by a change in the flow structure initiated by a change in one of the cooling mass flows ($\dot{m}_2$ or $\dot{m}_3$). This is possible because in equation (9), Γ_{vane} is a function of both p_{exit}/p_{01} *and*—crucially—p_{02}/p_{01}. The advantage of equation (9) lies primarily in the fact that it is explicitly expressed as a function of these two pressure ratios.

We feel that this justifies, for most purposes, defining NGV capacity in the form of equation (9)—it is sufficiently complete (on account of Γ_{vane} being a function of both p_{exit}/p_{01} and p_{02}/p_{01}) to allow sensitivities to, for example, trailing edge coolant flow to be included inherently in the definition. It is noted that there is weak physical justification for the complete lack of mixing of streams 1 and 2, but it is felt that this is sufficiently compensated for by the explicit inclusion of the sensitivity to p_{02}/p_{01}. Recall that the purpose here is to select, from a range of apparently arbitrary possibilities, a capacity definition that is as robust and transportable between different environments as possible. The objective is not to develop a quasi-analytical model,[4] as there is, of course, no physical description of the flow within this framework.

Evaluation of vane capacity characteristic

A capacity characteristic for a test vane can be generated, in principle, from a single test in blowdown mode operation. In practice, a number of repeat tests are performed, both to reduce the precision error in the mean of the characteristic and to allow

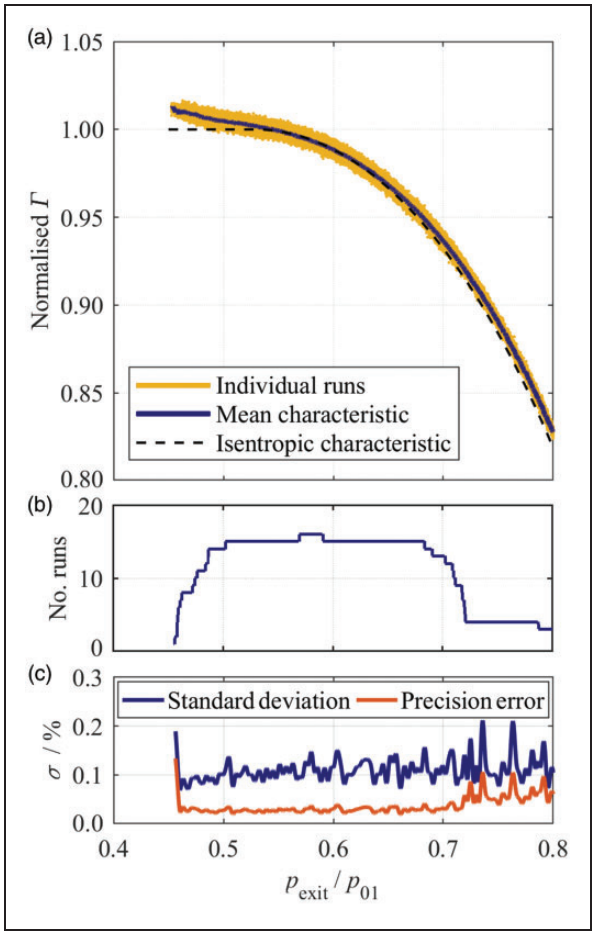

Figure 16. (a) Capacity characteristics from a typical HP NGV showing 17 repeat runs, and the mean-line trend; (b) number of repeat tests conducted as a function of p_{exit}/p_{01}; (c) standard deviation and precision uncertainty in the mean capacity trend.

this precision error to be evaluated. In this section, data from a typical set of experiments is presented and the method of generating a mean characteristic is demonstrated.

In this particular set, a total of 17 individual tests were conducted, shown by yellow lines in Figure 16(a). The mean capacity characteristic is overlaid in blue. Capacity is defined as in equation (9). Mass flow rates and vane inlet conditions of total pressure and temperature for each of the three constituent streams (mainstream, hub and case coolant) are measured as described in the preceding sections. The data are normalised with respect to the value at the nominal choked condition ($p_{exit}/p_{01} = 0.5283$).

To produce the mean characteristic, the data from all of the individual runs were resampled onto a uniform pressure ratio grid, allowing an unbiased mean to be computed. Individual runs had different ranges of p_{exit}/p_{01}. The number of individual runs covering each value of pressure ratio is plotted in Figure 16(b). The standard deviation of individual capacity characteristics from the mean characteristic, and the corresponding standard error in the mean are plotted in Figure 16(c) as functions of the mean vane pressure ratio, p_{exit}/p_{01}. Over the engine range of pressure ratio (typically $0.53 < p_{exit}/p_{01} < 0.65$), the standard deviation of individual capacity runs was 0.109% and the standard error in the mean ±0.025%. This is a low value, and is a small contributor to the overall uncertainty in capacity.

The capacity characteristic is, to first order, that of the classical isentropic trend (shown by the dashed curve in Figure 16a). In contrast to the isentropic trend, however, after reaching a near-plateau at around the critical vane pressure ratio ($p_{exit}/p_{01} \approx 0.5283$), when p_{exit}/p_{01} is further reduced the value of capacity continues to rise relatively steeply. By a pressure ratio of $p_{exit}/p_{01} = 0.45$, capacity has risen by 0.84% relative to the critical pressure ratio (similar effect seen in Povey et al.,[3,6,7]). In this transonic region of the characteristic, the flow field through the controlling region of the passage is complex, with relatively strong trailing edge shocks, and unsteady effects due to vortex shedding from the trailing edge.

Evaluation of bias uncertainty in capacity measurement

The bias uncertainty in a typical vane (or overall) capacity measurement (defined as in equation (9)) is now considered. Capacity is a derived (as opposed to directly measured) variable. Evaluating its bias uncertainty therefore follows several stages. Before the bias uncertainty in capacity can be evaluated, the bias uncertainty in the following quantities must be determined:

i. The mass flow metering nozzle effective areas;
ii. The measured inlet feed mass flow rates;
iii. The unsteady mass flow correction term for each individual mass flow rate;
iv. The vane inlet total pressure for each individual stream;
v. The vane inlet total temperature for each individual stream.

Error propagation techniques are then used to calculate the bias uncertainty in:

vi. The individual stream capacity terms (three terms on the right hand side of equation (9);
vii. The total vane capacity (left hand side of equation (9)).

Once the bias uncertainty in the total vane capacity has been obtained, the additional contributions to bias uncertainty arising from the following sources are considered:

viii. Uncertainty in the evaluation of the mean vane operating pressure ratio, p_{exit}/p_{01};
ix. Uncertainty in the evaluation of the coolant-to-mainstream pressure ratio, p_{02}/p_{01}.

The analysis is now progressed through the preceding nine stages. All bias uncertainty figures are given to 95% confidence. To frame the discussion around a particular example, a typical cold-rig test case is considered with the conditions listed in Table 4. The values of bias, precision, and overall uncertainties in vane capacity obtained from this analysis are then summarised and compared against those achieved in the original facility (the uncertainty analysis for which can be found in Povey et al.[6]), and a proposed upgraded facility. The latter differs from the current facility only in that the mainstream mass flow metering nozzle will be calibrated to ±0.250% bias uncertainty in effective area. All other parts of the measurement chain remain unchanged.

(i) Bias uncertainty in mass flow metering nozzle effective areas

The mainstream is fed with a sonic Venturi nozzle, operated at choked pressure ratios. The nozzle was calibrated to a bias uncertainty in the effective area, A_m, of ±0.500% (95% confidence). That is, $\sigma^{\%}_{A_m} = \pm 0.500\%$.

The hub and case coolant streams are fed from separate choked Venturi nozzles. The nozzle diameters used were approximately 16.0 mm and 15.3 mm for the hub and case, respectively. The estimated bias uncertainty in the coolant nozzle diameters is ±0.05 mm, or $\sigma^{\%}_{D_h} = \pm 0.313\%$ for the hub nozzle and $\sigma^{\%}_{D_c} = \pm 0.327\%$ for the case nozzle. The discharge coefficient in both cases was taken from ISO 9300[9] to be $C_d = 0.993$. The uncertainty in C_d was established to be negligible in relation to that in the nozzle diameters (less than ±0.001%). The estimated bias uncertainties in the coolant nozzle effective areas are therefore given by: $\sigma^{\%}_{A_h} = \pm 0.626\%$, and $\sigma^{\%}_{A_c} = \pm 0.654\%$.

(ii) Bias uncertainty in mass flow measurements

The mass flow rate through a choked Venturi nozzle is a function of the nozzle effective area and the upstream total pressure and temperature. First, consider the mainstream nozzle. The relationship is given by

$$\dot{m}_m \propto A_m p_{0,m} \sqrt{T_{0,m}} \tag{10}$$

where $p_{0,m}$ and $T_{0,m}$ are the total pressure and temperature upstream of the nozzle, respectively. For completeness, note there is also a weak dependence on gas properties, γ and R. This is estimated to be small (bias uncertainty below 0.01%) in the typical cold-rig situation and is ignored in this analysis.

The general equation for propagation of percentage uncertainty from directly measured to derived quantities is given in equation (21) in Appendix 1. For this case we get

$$\sigma^{\%}_{\dot{m}_m} = \left[\sigma^{\%\,2}_{A_m} + \sigma^{\%\,2}_{p_{0m}} + \tfrac{1}{4}\sigma^{\%\,2}_{T_{0m}} \right]^{1/2} \tag{11}$$

The total pressure upstream of the main nozzle (nominal value 12.0 bar) was measured by two 30 bar transducers with quoted bias uncertainty (combined non-linearity and hysteresis) of ±0.04% of the transducer range. The uncertainty in the average measurement was therefore given by $0.04\% \times (30.0/12.0)/\sqrt{2} = \pm 0.071\%$.

The total temperature upstream of the main nozzle (nominal value 268 K) was measured using eight 0.025 mm K-type bare-bead thermocouples, with a quoted measurement accuracy of ±1.5 K, or ±0.560%. The percentage uncertainty in the average temperature measurement was therefore $0.56\%/\sqrt{8} = \pm 0.198\%$. The additional uncertainty associated with the thermal dissimilarity (to the calibration experiment) of the nozzle boundary layer due to the nonisothermal nature of the blowdown test can be shown to be very small and is ignored. The bias uncertainty in the primary nozzle mass flow rate measurement is then obtained by substituting the computed uncertainties into equation (9). This gives $\sigma^{\%}_{\dot{m}_m} = \pm 0.515\%$.

$\sigma^{\%}_{\dot{m}_m}$ is dominated by the uncertainty in the primary nozzle calibration. It is now possible (with state-of-the-art calibration techniques) to improve the calibration accuracy from ±0.500% to ±0.250%. The implications of this for experimental capacity measurement are discussed at the end of this paper. The corresponding bias uncertainties in the hub and case coolant nozzle mass flow rates are calculated in the same way. The uncertainties are summarised in Table 5.

(iii) Bias uncertainty arising from unsteady mass flow correction terms

Mass accumulation in the intermediate plena between the metering nozzles and the vane (due to changing pressure and temperature) creates a small difference between the mass flow rates delivered to the vane by each of the three streams, and the mass flow rates

Table 4. Summary of conditions for example capacity test case.

p_{exit}/p_{01}	T_{01}/T_{02}	p_{01}/p_{02}	$\dot{m}'_h/\dot{m}'_{total}$	$\dot{m}'_c/\dot{m}'_{total}$
0.55	1.0	1.025	0.039	0.036

Table 5. Summary of bias uncertainties in coolant stream pressures, temperatures and mass flow rates.

Stream	$\sigma^{\%}_{p_0}$	$\sigma^{\%}_{T_0}$	$\sigma^{\%}_{\dot{m}}$
Hub coolant	±0.292%	±0.270%	±0.703%
Case coolant	±0.292%	±0.270%	±0.728%

measured at the corresponding metering nozzles. The measured mass flow rates are corrected for this effect, as discussed in the earlier section.

Again taking the mainstream feed as an example, the mass flow rate delivered to the vane, $\dot{m}'_{\mathrm{m}}$, is given by

$$\dot{m}'_{\mathrm{m}} = \dot{m}_{\mathrm{m}} + \dot{m}''_{\mathrm{m}} = \dot{m}_{\mathrm{m}} + \sum_{i=1}^{4} \dot{m}''_{\mathrm{i}} \tag{12}$$

where $\dot{m}_{\mathrm{m}}$ is the mass flow rate measured at the mainstream nozzle and $\dot{m}''_{\mathrm{m}}$ is the correction term. $\dot{m}''_{\mathrm{m}}$ can be expressed as a summation over the intervening plena—in this case the sum over $i = 1$–4 of the correction terms, for the arbitrarily segmented description of the mainstream feed system (see Figure 1).

The unsteady mass flow correction term for each of the intermediate plena V1–V6 is computed based on equation (2): $\dot{m}'' = f\,(V_i,\ p_i,\ T_i,\ \mathrm{d}p_i/\mathrm{d}t,\ \mathrm{d}T_i/\mathrm{d}t)$, where the subscript i denotes an individual plenum. The volumes of the intermediate plena were measured to an estimated accuracy of ±5%. Uncertainties in the rates of change of plenum pressures and temperatures ($\mathrm{d}p_i/\mathrm{d}t$, $\mathrm{d}T_i/\mathrm{d}t$) were estimated conservatively to be of order ±15%. This is a high degree of uncertainty compared to the directly measured quantities and therefore dominates the estimated uncertainties in the correction mass flow rates.

Applying the general equation for uncertainty propagation (equation (21) in Appendix 1) to the expression for the plenum mass flow correction term (equation (2)), an expression is derived for the estimated bias uncertainty in the mass flow correction term for a single plenum

$$\sigma^{\%}_{\dot{m}''_i} = \left[\begin{array}{l} \left(\frac{V_i}{\dot{m}''_i RT_i}\right)^2 \left(\frac{\mathrm{d}p_i}{\mathrm{d}t} - \frac{p_i}{T_i}\frac{\mathrm{d}T_i}{\mathrm{d}t}\right)^2 \sigma^{\%2}_{V_i} \\ \quad + \left(\frac{p_i V_i}{\dot{m}''_i RT_i^2}\frac{\mathrm{d}T_i}{\mathrm{d}t}\right)^2 \sigma^{\%2}_{p_i} \\ \quad + \left(\frac{V_i}{\dot{m}''_i RT_i}\right)^2 \left(\frac{2p_i}{T_i}\frac{\mathrm{d}T_i}{\mathrm{d}t} - \frac{\mathrm{d}p_i}{\mathrm{d}t}\right)^2 \sigma^{\%2}_{T_i} \\ + \left(\frac{V_i}{\dot{m}''_i RT_i}\frac{\mathrm{d}p_i}{\mathrm{d}t}\right)^2 \sigma^{\%2}_{\frac{\mathrm{d}p_i}{\mathrm{d}t}} + \left(\frac{p_i V_i}{\dot{m}''_i RT_i^2}\frac{\mathrm{d}T_i}{\mathrm{d}t}\right)^2 \sigma^{\%2}_{\frac{\mathrm{d}T_i}{\mathrm{d}t}} \end{array} \right]^{1/2} \tag{13}$$

The individual plenum correction terms are estimated and then the uncertainty in the total mainstream correction mass flow rate is determined by summing the terms for plena V1–V4

$$\sigma^{\%}_{\dot{m}''_{\mathrm{m}}} = \left[\sum_{i=1}^{4} \left(\frac{\dot{m}''_i}{\dot{m}''_{\mathrm{m}}}\right)^2 \sigma^{\%2}_{\dot{m}_i} \right]^{1/2} \tag{14}$$

The correction flow rates for the hub and case coolant streams require terms for plena V6 and V5 respectively. Results for a typical test are summarised in Table 6. The result of applying the unsteady correction is to marginally increase the uncertainty in mainstream mass flow rate (from ±0.515% to ±0.530%). The coolant stream mass flow rates are only marginally affected. Curiously, the uncertainty of the corrected hub coolant flow rate is very slightly smaller than the corresponding uncertainty for the uncorrected flow rate. This surprising result arises from the statistical process of combining uncertainties, and is discussed in detail in Appendix 1.

Table 6. Summary of typical mainstream, hub and case coolant correction mass flow rates and estimated bias uncertainties.

Flow stream Plena	Mainstream V1–V4	Case coolant V5	Hub coolant V6
$\dot{m}$ / kg s^{-1}	13.120	0.519	0.561
$\dot{m}''$ / kg s^{-1}	0.149	0.003	0.002
$\dot{m}'$ / kg s^{-1}	13.269	0.521	0.563
$\sigma^{\%}_{\dot{m}}$	±0.515%	±0.728%	±0.703%
$\sigma^{\%}_{\dot{m}''}$	±13.09%	±11.42%	±16.03%
$\sigma^{\%}_{\dot{m}'}$	±0.531%	±0.729%	±0.702%

(iv) Bias uncertainty in inlet total pressure measurements

The mainstream total pressure at vane inlet (nominal value 2.0 bar) is measured using 32 transducers of range 5 bar, with quoted bias uncertainty of ±0.1% of full-scale range. The bias uncertainty in a single measurement was therefore 0.1 (5.0/2.00) = ±0.250%. The bias uncertainty in the mean of all 32 measurements was therefore $\sigma^{\%}_{p_{0\mathrm{m}}} = 0.250\%/\sqrt{32} = \pm 0.044\%$.

The standard deviation of the 32 individual measurements at a representative single point during a test was ±0.187%. This is within the ±0.250% bias uncertainty expected in an individual measurement due to the transducer specification. Hence, the spatial non-uniformity in inlet total pressure is extremely small.

Hub and case coolant total pressures are measured in the coolant cavities within the vane module in the form of differential measurements relative to the mainstream vane inlet total pressure. The nominal coolant-to-mainstream pressure differential was 0.050 bar. The differentials at hub and case were measured by five and four ±0.350 bar differential transducers, respectively, with quoted bias uncertainty due to non-linearity and hysteresis of ±0.2% of the full-scale range. The estimated percentage bias uncertainties in total pressure are calculated as $\sigma^{\%}_{p_{0,\mathrm{h}}} = \pm 0.626\%$ and $\sigma^{\%}_{p_{0,\mathrm{c}}} = \pm 0.700\%$ for the hub and case, respectively. Here Δp_0 refers to the coolant-to-mainstream pressure *differential*.

The bias uncertainty in the *absolute* values of coolant inlet total pressure is dominated by the mainstream total pressure measurement due to the small

relative size of the pressure differential. Bias uncertainty is computed as $\sigma^{\%}_{p_{0\mathrm{hc}}} = \sigma^{\%}_{p_{0\mathrm{cc}}} = \pm 0.046\%$ for both the hub and case streams.

(v) Bias uncertainty in inlet total temperature measurements

Mainstream total temperature at vane inlet (nominal value 277 K) is measured by 32 K-type thermocouples, each with a quoted measurement accuracy of ±1.5 K or ±0.540% bias uncertainty. The bias uncertainty in the mean of all 32 measurements was therefore $\sigma^{\%}_{T_{0\mathrm{m}}} = 0.540\%/\sqrt{32} = \pm 0.096\%$.

The standard deviation of the 32 individual measurements at a representative single point during a test was ±0.074%. This is small in comparison to the ±0.540% bias uncertainty in the individual measurements, indicating that the spatial non-uniformity in inlet total temperature is negligible. For completeness, note that the assumption that all of the individual measurements are entirely independent is unlikely to be true in practice, as the instruments come from a common batch and thus their bias uncertainties will be partially correlated.

Hub and case coolant stream total temperatures are measured in the coolant cavities within the vane module, by five and four K-type thermocouples, respectively. The bias uncertainties are therefore determined as $\sigma^{\%}_{T_{0\mathrm{h}}} = \pm 0.241\%$ and $\sigma^{\%}_{T_{0\mathrm{c}}} = \pm 0.270\%$.

(vi) Bias uncertainty in individual stream capacity terms

The bias uncertainties in mass flow rate, inlet total pressure and total temperature are now combined to calculate the bias uncertainty in capacity. This is done for each of the mainstream, hub and case coolant streams, represented by the three terms on the right-hand side of equation (9). As an example, the bias uncertainty in the mainstream capacity term, Γ_{m}, is given by

$$\sigma^{\%}_{\Gamma_{\mathrm{m}}} = \left[\sigma^{\%\ 2}_{\dot{m}'_{\mathrm{m}}} + \sigma^{\%\ 2}_{p_{0\mathrm{m}}} + \frac{1}{4}\sigma^{\%\ 2}_{T_{0\mathrm{m}}} \right]^{1/2} \tag{15}$$

Substituting in numbers gives $\sigma^{\%}_{\Gamma_{\mathrm{m}}} = \pm 0.534\%$. Comparing the uncertainty in the mainstream capacity term to the uncertainty in the corresponding mass flow term, $\sigma^{\%}_{\dot{m}'_m} = \pm 0.530\%$, shows that the difference arising from the measurement of mainstream cascade inlet flow conditions is only 0.004%—a very small value. This indicates that instrumentation of the mainstream vane inlet flow conditions is optimised. The bias uncertainty of the hub and case coolant capacity terms are determined in the same way, giving $\sigma^{\%}_{\Gamma_{\mathrm{h}}} = \pm 0.714\%$ and $\sigma^{\%}_{\Gamma_{\mathrm{c}}} = \pm 0.743\%$, respectively.

The difference in uncertainty between the individual coolant stream mass flow rate and capacity terms is therefore ±0.012% for the hub and ±0.014% for the case. This is driven primarily by the bias uncertainty in coolant feed total temperature measurements. There is little to gain from further optimisation of stream inlet total pressure instrumentation.

(vii) Bias uncertainty in overall capacity measurement

The bias uncertainties associated with the individual capacity terms are now combined to calculate the uncertainty in the overall capacity (definition of equation (9)), as follows

$$\sigma^{\%}_{\Gamma_{\mathrm{vane}}} = \left[\left(\frac{\Gamma_{\mathrm{m}}}{\Gamma_{\mathrm{vane}}}\right)^2 \sigma^{\%^2}_{\Gamma_{\mathrm{m}}} + \left(\frac{\Gamma_{\mathrm{h}}}{\Gamma_{\mathrm{vane}}}\right)^2 \sigma^{\%^2}_{\Gamma_{\mathrm{h}}} + \left(\frac{\Gamma_{\mathrm{c}}}{\Gamma_{\mathrm{vane}}}\right)^2 \sigma^{\%^2}_{\Gamma_{\mathrm{c}}} \right]^{1/2} \tag{16}$$

Substituting in the previously computed values gives $\sigma^{\%}_{\Gamma_{\mathrm{vane}}} = \pm 0.494\%$. The *percentage* uncertainty (but not the absolute uncertainty) in the sum is lower than that in any of the constituent measurements. The small reduction arises because the measurements are assumed to be entirely independent. The mathematical basis for this effect is discussed in Appendix 1.

(viii) Bias uncertainty in capacity due to uncertainty in exit static pressure and vane pressure ratio

The overall capacity defined in equation (9) is a function of two controlling pressure ratios: p_{exit}/p_{01} and p_{02}/p_{01}. This can be visualised as a surface in the pressure ratio space (Figure 12). Measurement error in either p_{exit}/p_{01} or p_{02}/p_{01} leads to error in the evaluation of vane capacity. The magnitude of this error is proportional to the local gradient of the function $\Gamma_{\mathrm{vane}}(p_{\mathrm{exit}}/p_{01}, p_{02}/p_{01})$ in the relevant axis (i.e. the partial derivative in a particular direction). Each of these pressure ratio axes is now considered in turn.

Uncertainty in the measurement of mean static pressure at vane exit, p_{exit}, leads to error in the evaluation of the pressure ratio p_{exit}/p_{01}. This can be thought of as a movement over the capacity surface in the $(p_{\mathrm{exit}}/p_{01})$-direction (see Figure 12). Recall that static pressure at vane exit is measured experimentally by a total of 96 tappings located on the vane platforms at hub and case, a short distance downstream of the vane trailing edges (Figure 7). The definition of vane exit static pressure is somewhat arbitrary. In principle, one could determine an accurate area-average or mass-flow-average static pressure by traversing, but this would be impractical and possibly subject to probe interference effects. Even if it were desired, it would only be possible at a downstream plane—defining a unique *controlling area* here that was related to the measurement would not be possible. In short, it

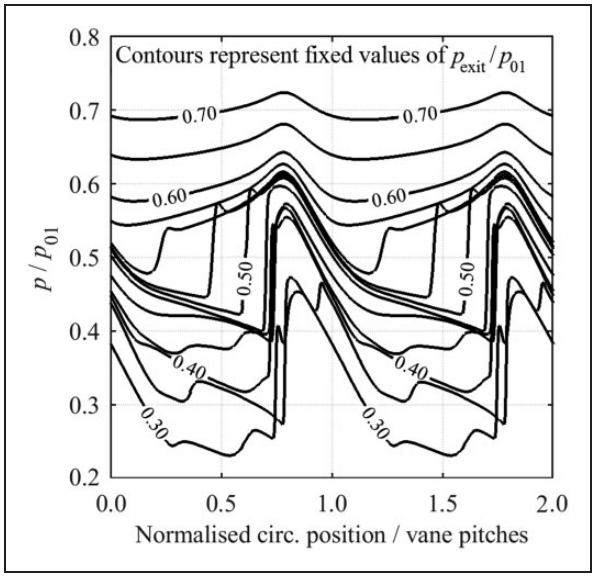

Figure 17. CFD-predicted circumferential static pressure profiles at vane exit (single axial position) for a range of operating pressure ratios.

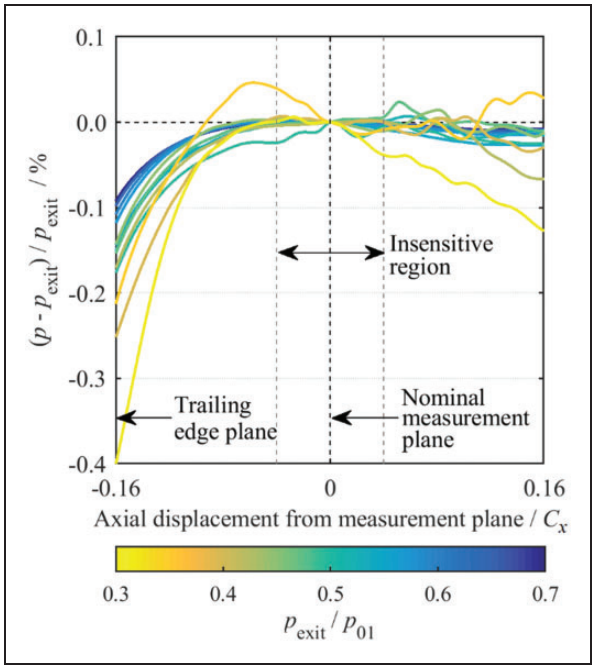

Figure 18. CFD-predicted variation in circumferentially averaged pressure ratio as a function of axial interrogation plane for a range of p_{exit}/p_{01}.

is hard to see any advantage in measuring static pressure by traversing, and there are a number of possible disadvantages that would need to be considered.

Likewise, in principle a vane exit static pressure could be defined based on a single tapping measurement. This would likely lead to an unusual capacity characteristic, as the flow structure (exact location and strength of shocks etc.) close to the tapping location would change with vane pressure ratio, thus distorting the x-axis of the characteristic. A more significant problem would be the sensitivity to the exact tapping location, and the difficulty of replicating the precise position in a corresponding CFD study or repeat experiment. The aim—as far as capacity measurement is concerned—is to define a static pressure measurement protocol which is robust between repeat experiments, different builds of the same experiment, and in comparisons against computational simulations.

The sensitivity of capacity to the vane exit static pressure measurement is now examined using 2D Reynolds-Averaged Navier-Stokes (RANS) simulations. The profile is based on a section of the vane at midspan. Results of the simulation are presented in Figures 17 and 18.

Circumferential static pressure distributions at vane exit are plotted in Figure 17 for 13 values of mean vane pressure ratio in the range $0.30 \leqslant p_{exit}/p_{01} \leqslant 0.70$. The data were extracted (from CFD) at the same axial location as the experimental measurement points, 0.17 axial chords downstream of the vane trailing edge. Corresponding experimental data for a single pressure ratio were shown in Figure 8. As p_{exit}/p_{01} is decreased, the circumferential non-uniformity in the profile increases. For $p_{exit}/p_{01} \leqslant 0.55$, a shock crosses the measurement plane, marked by a high gradient of static pressure. As p_{exit}/p_{01} decreases, the shock strengthens and moves rightwards. This profile is characteristic of forward loaded HP NGVs.

At each value of p_{exit}/p_{01} (representing an individual CFD solution), the static pressure distributions in the underlying data (Figure 17) are circumferentially averaged *at each axial location* to give a single value. The trends in the axial direction of this circumferential average are presented in Figure 18 as functions of pressure ratio (p_{exit}/p_{01}). A range of axial positon $|x/C_x| < 0.16$ has been considered, centred on the nominal measurement plane ($x/C_x = 0$). At a particular value of p_{exit}/p_{01} based on the nominal measurement plane, the circumferentially averaged values of p_{exit}/p_{01} at each axial location (in the range $|x/C_x| < 0.16$) are expressed as a percentage difference from the value at the nominal measurement plane ($x/C_x = 0$).

With the exception of very low pressure ratios ($p_{exit}/p_{01} < 0.4$), the axial gradient of average static pressure close to the measurement plane ($|x/C_x| < 0.05$) is extremely small (variation of less than 0.03%), showing very low sensitivity to small axial deviations in tapping location. Further downstream ($x/C_x > 0.05$), a complex shock system develops in the flow field, causing an increase in the sensitivity to the choice of axial measurement plane. This will be returned to in the context of defining an optimum distribution of tappings (axial and circumferential locations) for capacity measurement.

Before determining an optimum practicable distribution of pressure tappings, three principal sources of bias uncertainty affecting the evaluation of a robust mean vane exit static pressure are examined. These are:

(a) Discrete sampling (limited number of tappings) of the time-varying, spatially non-uniform static pressure field at vane exit, which features complex flow features with high gradients. This is referred to as *uncertainty due to tapping pattern*.
(b) Uncertainty in the location of tappings, arising due to variation in the vane manufacture and/or inaccuracies in the positioning of the tappings. This is referred to as *uncertainty due to variation in tapping location*.
(c) Uncertainty in the measurement of static pressure at each tapping due to pressure transducer bias uncertainty. This is referred to as *transducer measurement uncertainty*.

Each of these sources of error is now dealt with in turn.

Uncertainty due to tapping pattern arises due to the sensitivity of the mean vane exit static pressure measurement to the tapping pattern. The error is defined as the difference between the arithmetic mean of the static pressure values at the finite set of tapping locations, and the underlying circumferential average pressure. Taking this definition, the uncertainty due to tapping pattern depends on both the number of measurement points, and on their circumferential locations relative to the underlying flow field. Certain measurement points will sit in particularly high pressure gradients in the flow—for example a tapping sitting in the path of a shock which moves across the tapping location with changing vane pressure ratio. Other tappings will be located in less sensitive regions of the flow, closer to mid-passage, for example, or in regions which (over a normal operating pressure range) remain on one side or another of a shock. By increasing the number of tappings, these sensitivities are averaged out.

Using the data of Figure 17, the uncertainty due to tapping pattern is estimated by considering the difference between the average pressure measured by a *particular number* of evenly spaced circumferential sample points and the underlying circumferentially averaged pressure. For a given number of tappings, the maximum difference is found by considering every possible circumferential positioning. This is referred to as the *worst-case* error. In Figure 19, the worst-case error, normalised by $p_{01} - p_{exit}$ (y-axis), is plotted as a function of vane pressure ratio over the range $0.30 \leqslant p_{exit}/p_{01} \leqslant 0.70$ (x-axis), for a number of sample points between two and eight.

The worst-case error is approximately inversely proportional to the number of sample points. This result is expected as the average of an increasing number of discrete samples converges on the continuous average.

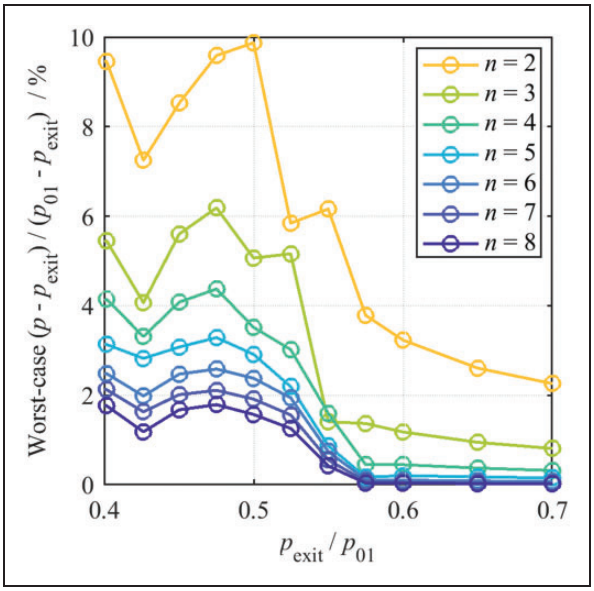

Figure 19. Normalised maximum difference between the underlying circumferentially-averaged pressure, and the average pressure as measured by a particular number of evenly spaced circumferential sample points. Each line represents a different number of sample points.

The trend with decreasing pressure ratio (p_{exit}/p_{01}) shows a sharp rise in the maximum pressure difference as the flow enters the transonic region. This is due to the presence of shocks, which cause high gradients in static pressure (see Figure 17). A typical experimental campaign has eight tappings per vane pitch (see Figure 7). From Figure 19, for $n = 8$, at a nominal vane pressure ratio of $p_{exit}/p_{01} = 0.55$, the normalised worst case error is approximately $\pm 0.417\%$. This gives a (non-normalised) worst case bias uncertainty in p_{exit} due to tapping pattern of $\pm 0.327\%$.

Uncertainty due to tapping location variation arises due to the sensitivity of the mean vane exit static pressure measurement to deviations of individual static tappings from their intended locations on the vane platforms. To estimate the uncertainty arising from this effect, the location of each sample point in the CFD model is allowed to move both circumferentially and axially. The range of possible deviations was estimated very pessimistically to be ± 1.5 mm in both directions. The position of a given tapping is then represented by a 2D normal distribution in space, with 95% of samples lying within ± 1.5 mm of the nominal location. At each vane pressure ratio, the distribution of each pressure measurement corresponding to the 2D normal distribution for the tapping was then evaluated by interpolating the underlying predicted 2D flow field (visualised in 1D in Figures 17 and 18). Thus, a probability density function (PDF) is determined to describe the expected static pressure measured at a given tapping. These functions vary greatly from tapping to tapping, in some cases being similar to skewed normal distributions, and in others being bimodal (in the vicinity of a

shock, for example). Uncertainty bounds on the value at each tapping are determined to the 95% *credible interval* (the interval within which 95% of samples are expected to fall, given that the true, underlying PDF is known) at each value of p_{exit}/p_{01}. Sample points located close to shocks have a larger credible interval due to high spatial pressure gradients within the region in which the sample could lie.

For each particular tapping distribution (particular number of tappings and circumferential positioning), the PDF and associated credible interval for the pitch-wise-average static pressure are calculated by considering the PDF and associated credible interval for each individual tapping location. In each case, the maximum credible interval is taken from all possible circumferential locations of the sample points (similar analysis to that used to evaluate the pattern location uncertainty). The size of the credible interval for p_{exit} defines the uncertainty in p_{exit} due to tapping location uncertainty.

The worst-case (across all possible circumferential positions of a given number of samples) credible interval for the inferred value of p_{exit} is plotted in Figure 20 as a function of both p_{exit}/p_{01} and the number of sample points. For a given value of p_{exit}/p_{01}, increasing the number of samples significantly reduces the size of the credible interval, as the averaging effect causes the inferred average pressure to become increasingly insensitive to particularly high gradients in the flow field. The worst-case credible interval grows substantially as p_{exit}/p_{01} passes through the transonic range into the mildly supersonic range. This is due to the presence of strong pressure gradients across shockwaves. At low p_{exit}/p_{01}, the uncertainty due to tapping location variation is reduced significantly by increasing the number of sample points. At high p_{exit}/p_{01}, a larger number of tappings is less important as the flow field is more uniform.

A typical experimental campaign has eight tappings per vane pitch (see Figure 7). From Figure 20, at a nominal vane pressure ratio of $p_{exit}/p_{01} = 0.55$, the normalised credible interval for the inferred average pressure value is therefore approximately 0.864%. This gives a (non-normalised) worst case error in p_{exit} due to tapping location variation of ±0.407%. This uncertainty is mitigated by the use of several instrumented vanes (three vane pairs or twelve instrumented platforms in a typical experiment in the current facility). Assuming the positioning of tappings on each platform to be independent, the bias uncertainty in p_{exit} based on 12 platforms is given by $0.407/\sqrt{12} = \pm 0.118\%$.

Finally, the contribution to the bias uncertainty in p_{exit} of *transducer measurement uncertainty* is considered. In a typical experiment in the current facility, the vane exit static pressure is measured using a total of 96 transducers (2 bar range) distributed over the 12 instrumented vane platforms. The quoted bias uncertainty was ±0.1% of transducer range, and the nominal operating pressure was 1.09 bar. The bias uncertainty in an individual measurement was

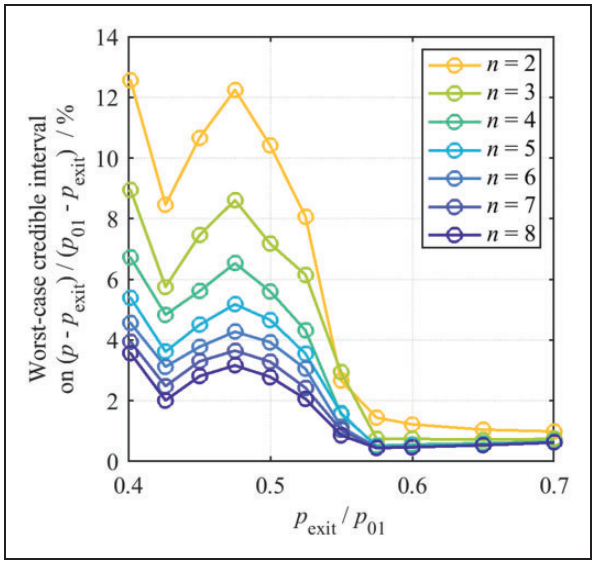

Figure 20. Normalised credible interval for average pressure measured by a particular number of—nominally—evenly spaced circumferential sample points subject to random spatial variation of ±1.5 mm both axially and circumferentially. Results are for a single instrumented platform. Each line represents a different number of samples.

therefore $0.1 \times (2.00/1.09) = \pm 0.184\%$. This gives a bias uncertainty in the mean pressure measured on a single vane platform (mean of eight measurements) of ±0.065%. The uncertainty in the mean pressure measured across all 12 platforms (mean of 96 measurements) was therefore 0.019%.

The overall bias uncertainty in the vane exit static pressure measurement is determined by combining the uncertainties arising from each of the three sources of uncertainty. The overall bias uncertainty is plotted as a function of p_{exit}/p_{01} in Figure 21. The contribution to the bias uncertainty of each of the three underlying sources of uncertainty is also shown. Dashed lines represent the result for an individual platform (eight tappings). Solid lines represent a typical experiment with 12 instrumented platforms. Note only one line is shown for tapping pattern uncertainty, which is independent of the number of platforms considered.

At the nominal pressure ratio ($p_{exit}/p_{01} = 0.55$), the overall bias uncertainty in p_{exit} associated with a single vane platform measurement is ±0.633%. The uncertainty associated with a measurement over 12 instrumented platforms is ±0.362%. This bias uncertainty is then combined with the previously evaluated bias uncertainty in vane inlet total pressure, p_{01}, to obtain the bias uncertainty in vane pressure ratio, p_{exit}/p_{01}. This gives $\sigma^{\%}_{\frac{p_{exit}}{p_{01}}} = \pm 0.365\%$.

The bias uncertainty in p_{exit}/p_{01} can be translated into a bias uncertainty in vane capacity by reference to the surface of capacity in pressure–ratio space, $\Gamma_{vane}(p_{exit}/p_{01}, p_{02}/p_{01})$. This was presented in Figure 12. In the figure the sensitivity to p_{02}/p_{01} was exaggerated for visualisation purposes. The underlying

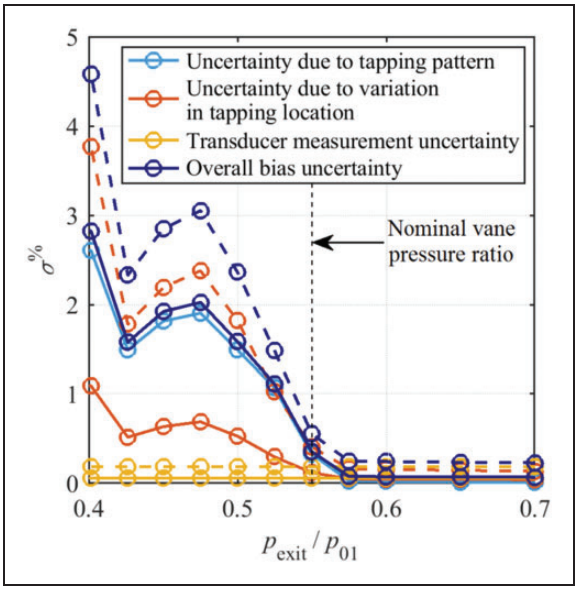

Figure 21. Bias uncertainty in p_{exit} from each of the three principal sources, along with the overall bias uncertainty, as functions of p_{exit}/p_{01}. Dashed and solid lines represent the uncertainties associated with single platform and 12 platform measurements, respectively.

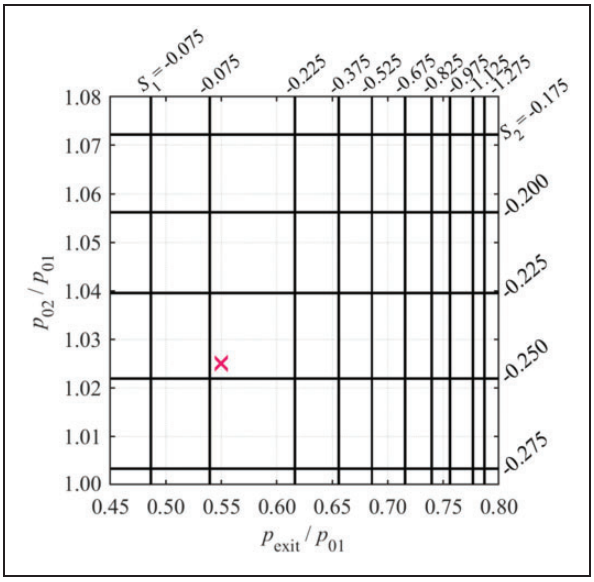

Figure 22. Contours of the sensitivity coefficients S_1 (defined in equation (17)) and S_2 (defined in equation (20)) as functions of p_{exit}/p_{01} and p_{02}/p_{01}.

(unexaggerated) data is now used to evaluate typical sensitivities in both axes. The sensitivity of $\Gamma_{vane}(p_{exit}/p_{01}, p_{02}/p_{01})$ to p_{exit}/p_{01}, which we call S_1, is defined in terms of the normalised partial derivative, as follows

$$S_1 = \frac{\partial \Gamma_{vane}\left(\frac{p_{exit}}{p_{01}}, \frac{p_{02}}{p_{01}}\right)}{\partial\left(\frac{p_{exit}}{p_{01}}\right)} \times \frac{\left(\frac{p_{exit}}{p_{01}}\right)}{\Gamma_{vane}} \tag{17}$$

Contours of S_1, along with a second sensitivity coefficient, S_2, which describes the sensitivity of capacity to p_{02}/p_{01}, are plotted in Figure 22. This will be returned to in the following section. The nominal operating point is marked by a red cross.

At the operating point, S_1 takes a value of approximately -0.092. This shows that the uncertainty in vane capacity is an order of magnitude lower than the uncertainty in p_{exit}/p_{01}. For a bias uncertainty in p_{exit}/p_{01} of $\pm 0.365\%$, the corresponding uncertainty in vane capacity is $\pm 0.034\%$. To calculate the impact on overall uncertainty in vane capacity, this is combined with the uncertainty in vane capacity arising from steps (i) to (vii)—above—to obtain

$$\sigma^{\%}_{\Gamma_{vane}} = \left(0.494^2 + 0.034^2\right)^{1/2} = \pm 0.495\% \tag{18}$$

That is, the additional impact of uncertainty in exit static pressure and vane pressure ratio increases the overall bias uncertainty in vane capacity from $\pm 0.494\%$ to $\pm 0.495\%$.

(ix) Bias uncertainty in capacity due to uncertainty in coolant-to-mainstream pressure ratio

The additional uncertainty in capacity due to uncertainty in coolant-to-mainstream pressure ratio, p_{02}/p_{01}, is now considered. Here p_{02} is defined as the mean of the hub and case coolant total pressures—these are similar in most engine scenarios.

The bias uncertainties in mainstream and coolant inlet total pressures have been calculated as $\pm 0.044\%$ and $\pm 0.046\%$, respectively. These quantities share a large common element, as the coolant pressure is measured as a differential relative to the mainstream—that is, $p_{02}/p_{01} = 1 + \Delta p_{0,c}/p_{01}$, where $\Delta p_{0,c}$ is the coolant-to-mainstream pressure differential. The resulting bias uncertainty in coolant-to-mainstream pressure ratio is determined according to equation (21)

$$\sigma^{\%}_{\frac{p_{02}}{p_{01}}} = \left(\frac{\Delta p_{0,h} + \Delta p_{0,c}}{p_{0,h} + p_{0,c}}\right)\left(\begin{array}{c}\sigma^{\%\ 2}_{p_{0,m}} + \frac{1}{4} \times \sigma^{\%\ 2}_{\Delta p_{0,h}} \\ + \frac{1}{4} \times \sigma^{\%\ 2}_{\Delta p_{0,c}}\end{array}\right)^{1/2} \tag{19}$$

Substituting in values gives $\sigma^{\%}_{\frac{p_{02}}{p_{01}}} = \pm 0.012\%$.

In the same manner as the prior analysis, the bias uncertainty in p_{02}/p_{01} can be translated into a bias uncertainty in vane capacity by defining a sensitivity coefficient, S_2, which represents the sensitivity of $\Gamma_{vane}(p_{exit}/p_{01}, p_{02}/p_{01})$ to p_{02}/p_{01}, as follows

$$S_2 = \frac{\partial \Gamma_{vane}\left(\frac{p_{exit}}{p_{01}}, \frac{p_{02}}{p_{01}}\right)}{\partial\left(\frac{p_{02}}{p_{01}}\right)} \times \frac{\left(\frac{p_{02}}{p_{01}}\right)}{\Gamma_{vane}} \tag{20}$$

This sensitivity coefficient is plotted in Figure 22. At the operating point, the value of S_2 is approximately −0.246. That is, the uncertainty in vane capacity is reduced by a factor of around four relative to the uncertainty in p_{02}/p_{01}. For a bias uncertainty in p_{02}/p_{01} of ±0.012%, the corresponding uncertainty in vane capacity is of order ±0.003%.

To calculate the impact on overall uncertainty in vane capacity, this is combined with the uncertainty arising from steps (i) to (viii)—above—to obtain $\sigma^{\%}_{\Gamma_{\text{vane}}} = \pm 0.495\%$. That is, the uncertainty in p_{02}/p_{01} increases the overall uncertainty in vane capacity by a negligibly small amount.

Summary of uncertainties and comparison to original and proposed upgraded facilities

The bias uncertainties in mass flow rate and capacity measurements are now summarised and compared with the results both from the original facility (Povey et al.[6]), and a proposed upgraded facility.

Recall that—to a large extent—the overall uncertainty in mass flow rate and capacity measurements is driven by the bias uncertainty in the effective area of the primary (mainstream) metering nozzle. This is inherited from a calibration process (which gives a result traceable to an international standard) and cannot be improved by experimental technique. The uncertainty values for this term are given in the first row of Table 7. The other rows of the table should be referenced to these values.

The remaining rows of the table present the bias uncertainty in the mass flow rate measurements and capacity measurements of the three individual streams (mainstream, hub and case), and the bias uncertainty in the overall capacity measurement. The last is presented both excluding and including the errors associated with uncertainty in p_{exit}/p_{01} and p_{02}/p_{01}—parameters Γ_{vane} and Γ'_{vane}, respectively.

To calculate the overall uncertainty in capacity, the bias error must be combined with the precision uncertainty in the mean of the capacity characteristic. The latter is evaluated experimentally and has been discussed in the context of Figure 16. For the original facility, the standard deviation of individual capacity runs was ±0.040%. This gave a standard error in the mean (based on a typical campaign of approximately 20 runs) of ±0.028%. The corresponding values for the current facility are ±0.109% and ±0.025%, respectively. For the proposed upgraded facility, the same values are assumed. The values of overall uncertainty are summarised in Table 8.

Figure 23 provides visualisation of the propagation of bias uncertainty through the measurement and analysis chain, following the nine stages of analysis, i–ix, previously described. The original facility (described in detail by Povey et al.[6]) is shown by a blue line. The final bias uncertainty in capacity for this facility is ±0.536%.

The current facility is represented by red lines, with dotted lines indicating the coolant streams, and the solid line indicating the mainstream. The lines combine when the overall vane capacity is calculated (analysis stage vii.). The final bias uncertainty in capacity for this facility is ±0.495%. The primary improvements over the original facility come in steps vii and viii, leading to an improvement of ±0.040% in the final bias uncertainty in capacity. The yellow lines represent a proposed upgraded facility, differing from the current one only in that the calibration of the primary mass flow metering nozzle will be improved from ±0.500% bias uncertainty to ±0.250%. This results in a final bias uncertainty of ±0.301%.

The following conclusions regarding the uncertainty analysis are drawn:

- In the original facility, the entire measurement and analysis chain led to an *overall* uncertainty in capacity of ±0.536%, only ±0.036% greater than the ±0.500% bias uncertainty inherited from the primary nozzle. This was achieved by careful

Table 7. Comparison of *bias* uncertainties in mass flow rate and capacity measurements between: the original facility,[1] the current facility, and a proposed upgraded facility.

	Bias uncertainty (95%) / %		
Parameter	Original facility (Povey et al.[6])	Current facility	Proposed upgraded facility
A1	±0.500	±0.500	±0.250
$\dot{m}_m'$	±0.518	±0.530	±0.312
$\dot{m}_h'$	–	±0.702	±0.702
$\dot{m}_c'$	–	±0.729	±0.729
Γ_m	–	±0.534	±0.320
Γ_h	–	±0.714	±0.714
Γ_c	–	±0.743	±0.743
Γ_{vane}	±0.531	±0.494	±0.299
Γ'_{vane}	±0.535	±0.495	±0.301

Table 8. Comparison of *overall* uncertainties in capacity measurements between: the original facility,[6] the current facility, and a proposed upgraded facility.

	Original facility[1]	Current facility	Proposed upgraded facility
Γ'_{vane} bias	±0.535%	±0.495%	±0.301%
Γ'_{vane} precision (20 runs)	±0.028%	±0.025%	±0.025%
Γ'_{vane} overall	±0.536%	±0.496%	±0.302%

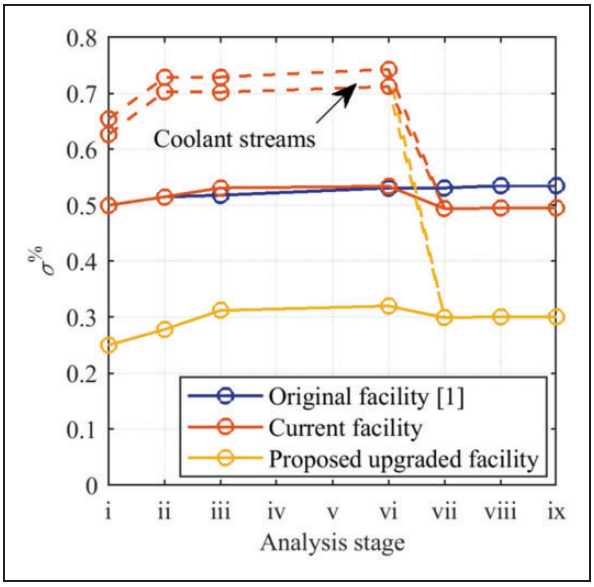

Figure 23. Visualisation of the propagation of bias uncertainty through to the final capacity measurement, for each of the three considered facilities.

experimental design in terms of hardware, instrumentation and experimental technique. Note that these values differ slightly from Povey et al.[6] as the bias uncertainty due to error in vane exit static pressure measurement is more comprehensively considered.

- In the current facility, a combination of small improvements in the measurement of inlet and exit flow conditions, and small refinements to the experimental technique have led to an *overall* uncertainty in capacity of ±0.496%, or ±0.004% *lower* than the ±0.500% bias uncertainty of the primary (mainstream) nozzle. This is possible because mainstream and coolant streams are independently metered. Figure 23 shows that the reduction in overall uncertainty relative to the original facility has two significant drivers: the independent measurement of coolant streams (approximately 8% of total flow), which has the curious effect of driving down the overall uncertainty (see Appendix 1); and a reduced uncertainty in p_{exit}/p_{01} due to increased number of vane exit static pressure measurements. These are analysis stages vii and viii. The improvement achieved is modest but noteworthy, and is justified by the importance of accurate capacity evaluation in the engine design and optimisation process.
- A proposed upgraded facility has been analysed which differs from the current facility only in the implementation of an improved calibration for the primary nozzle. This will reduce the *inherited* bias uncertainty from ±0.500% to ±0.250%. The *overall* uncertainty in capacity for this proposed upgraded facility will be ±0.302%, or ±0.052% greater than the bias uncertainty inherited from the primary nozzle. With a reduction in baseline uncertainty, the relative impact of the measurement and analysis chain (as described in stages ii–ix) will naturally be more significant. In particular, the measurement of flow conditions upstream of the primary nozzle (stage ii) and the application of the unsteady mass flow correction (stage iii) become significant contributors to overall uncertainty. It is felt that this facility would represent as optimal a system as practicable within realistic constraints.

Conclusions

In this paper, the current state-of-the-art in ultra-low uncertainty semi-transient techniques for experimental capacity measurement in gas turbines has been reviewed. A number of improvements to the technique, relative to previously published work, have been discussed. These improvements include: modularisation of the working section of such facilities to allow for rapid interchange of test vane modules; a move to independent metering of mainstream and coolant mass flow rates; and optimisation of instrumentation to minimise the measurement error in vane inlet and exit flow conditions.

A detailed uncertainty analysis has been presented which references the facility in which the technique was originally developed, the current facility, and a proposed future facility in which the uncertainty in capacity has been driven down to a practical limit using state-of-the-art nozzle calibration technology. The bias errors in vane capacity achieved by each of these three facilities are determined to be ±0.535%, ±0.495% and ±0.301%, respectively (to 95% confidence). The corresponding precision uncertainties are ±0.028%, ±0.025% and ±0.025%, respectively. The reduction in bias uncertainty between the original and current facilities was therefore ±0.040%. This is a small improvement but important in the context of the engine design and optimisation process. The combination of the extremely low precision uncertainty offered by the technique and the capability for rapid interchanging of test modules allows very small changes in capacity to be resolved. This facilitates studies of capacity sensitivity to secondary influences with much greater flexibility than was previously possible. In particular, studies of the effect of trailing edge coolant ejection, platform leakage flows, vane surface deterioration, and inlet flow disturbances (lean-burn combustor profiles) are topics of current interest.

The definition of vane capacity in systems with several streams at different inlet conditions of total pressure and temperature has been discussed. It is shown that whilst it is helpful for coolant stream mass flow rates and temperatures to be included in the capacity definition, the difference arising from the exact way in which this is achieved is minor. Whilst several definitions are similarly useful in terms of their robustness

to changes in the inlet conditions of individual streams, it is felt that the favoured definition offers the possibility—in the correct experiment—to isolate sensitivities to key effects such as trailing edge coolant ejection. This is achieved by explicitly expressing vane capacity as a function of the two key controlling pressure ratios. It is argued that this definition may be of more practical use when comparing results from different sources.

It is hoped that this paper will serve as a reference point for the current state-of-the-art in experimental gas turbine flow capacity measurement, and also as a manual for best practice in the development and analysis of experiments in this area.

Acknowledgment

The support of Rolls-Royce plc is gratefully acknowledged.

Declaration of Conflicting Interests

The author(s) declared no potential conflicts of interest with respect to the research, authorship, and/or publication of this article.

Funding

The author(s) received no financial support for the research, authorship, and/or publication of this article.

ORCID iD

Thomas Povey http://orcid.org/0000-0001-8977-9644

References

1. Raffel M and Kost F. Investigation of aerodynamic effects of coolant ejection at the trailing edge of a turbine blade model by PIV and pressure measurements. *Experiments Fluid* 1998; 24: 447–461.
2. Fielding L. The effect of irreversibility on the capacity of a turbine blade row. *Proc Inst Mech Eng* 1981; 195: 127–137.
3. Afanasiev IV, Granovskiy AV, Karelin AM, et al. Effect of 3D vane shape on the vane capacity. In: *Proceedings of ASME turbo expo 2004*, Vienna, Austria, 14–17 June 2004, Paper No. GT2004-53095.
4. Povey T. Effect of film cooling on turbine capacity. *ASME J Eng Gas Turbines Power* 2010; 132: 011901.
5. Kollen O and Koschel W. Effect of film cooling on the aerodynamic performance of a turbine cascade. Paper No. AGARD CP-390, 1985.
6. Povey T, Sharpe M and Rawlinson A. Experimental measurements of gas turbine flow capacity using a novel transient technique. *ASME J Turbomach* 2011; 133: 011005.
7. Hambidge C and Povey T. Numerical and analytical study of the effect of film cooling on HP NGV capacity. In: *Proceedings of ASME turbo expo 2012*, Copenhagen, Denmark, 11–15 June 2012, Paper No. GT2012-69066.
8. Kirollos B, Lubbock R, Beard P, et al. ECAT: an engine component aerothermal facility at the University of Oxford. In: *Proceedings of ASME Turbo Expo 2017*, Charlotte, NC, USA, 26–30 June 2017, Paper No. GT2017-64736.
9. British Standards Institution. *BS EN ISO 9300:2005 Measurement of gas flow by means of critical flow venturi nozzles*. London, UK: British Standards Institution, 2005.
10. Moffat RJ. Contributions to the theory of single-sample uncertainty analysis. *J Fluids Eng* 1982; 104: 250–258.

Appendix

Notation

A	area
A_{m}	effective area of mainstream Venturi nozzle
A_{h}	effective area of hub Venturi nozzle
A_{c}	effective area of case Venturi nozzle
C_d	discharge coefficient
C_x	axial chord length
c_p	specific heat capacity at constant pressure
D	diameter
F	arbitrary function used in Appendix
i	summation variable
K	arbitrary ratio used in Appendix
M	Mach number
$\dot{m}$	mass flow rate
$\dot{m}'$	mass flow rate delivered to NGV (corrected)
$\dot{m}''$	correction mass flow rate
$\dot{m}_{\mathrm{m}}$	mass flow rate measured at mainstream nozzle
$\dot{m}_{\mathrm{c}}$	mass flow rate measured at case coolant nozzle
$\dot{m}_{\mathrm{h}}$	mass flow rate measured at hub coolant nozzle
$\dot{m}_{\mathrm{total}}$	total mass flow rate (sum of $\dot{m}_m$, $\dot{m}_c$ and $\dot{m}_h$)
n	number of sample points per vane passage
p	pressure
$\overline{p_0}$	mass-flow averaged total pressure
p_{atm}	atmospheric pressure
p_{exit}	mean static pressure at vane exit
R	gas constant
S_1	sensitivity coefficient between capacity and vane pressure ratio
S_2	sensitivity coefficient between capacity and coolant-to-mainstream pressure ratio
T	temperature
$\overline{T_0}$	mass-flow averaged total temperature
t	time
V	plenum volume
x	arbitrary variable used in Appendix
y	arbitrary variable used in Appendix

Greeks

α	arbitrary uncertainty
Γ	capacity
Γ_{m}	mainstream capacity (component of Γ_{vane})
Γ_{h}	hub coolant stream capacity (component of Γ_{vane})
Γ_{c}	case coolant stream capacity (component of Γ_{vane})
Γ_{vane}	vane (or overall) capacity
γ	ratio of specific heat capacities
σ	uncertainty
$\sigma^{\%}$	percentage uncertainty
$\sigma^{\%}_{\Gamma_{\mathrm{vane}}}$	percentage uncertainty in vane capacity
$\sigma^{\%}_{\Gamma'_{\mathrm{vane}}}$	percentage uncertainty in vane capacity, including due to measurement of p_{exit}/p_{01} and p_{02}/p_{01}

Subscripts

0	stagnation condition
1	mainstream flow at cascade inlet
2	Film cooling flow at cascade inlet
3	trailing edge cooling flow at cascade inlet
c	case coolant stream
h	hub coolant stream
m	mainstream

Superscript

*	choked condition

Appendix 1. Propagation of uncertainty in a simple summation

For an arbitrary function of a set of entirely independent variables, for example $F=f(x, y,\ldots)$, the percentage bias uncertainty in the value of the function can be estimated from

$$\sigma_F^{\%} = \left[\left(\frac{\partial F}{\partial x}\right)^2 \frac{x^2}{F^2}\sigma_x^{\%2} + \left(\frac{\partial F}{\partial y}\right)^2 \frac{y^2}{F^2}\sigma_y^{\%2} + \ldots\right]^{1/2} \quad (21)$$

Let F be a simple summation of independent variables

$$F(x, y, \ldots) = x + y + \ldots \quad (22)$$

The partial derivative of F with respect to each of the variables x, y etc. is equal to unity, and the propagation equation for percentage uncertainty in F (equation (21)) simplifies to

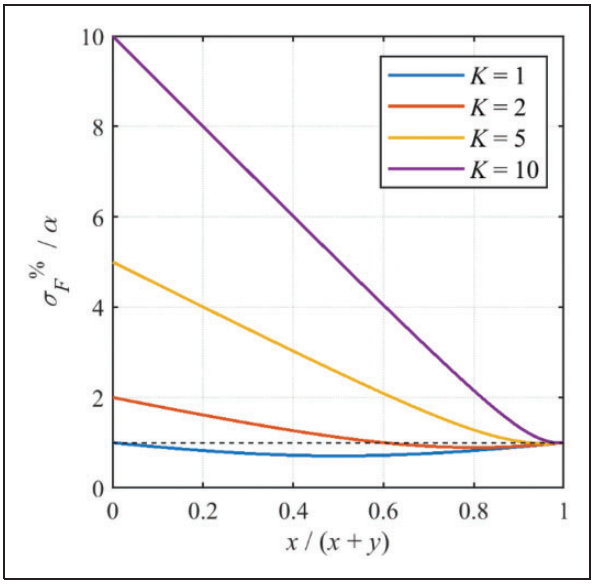

Figure 24. Percentage uncertainty in the sum of two variables, *x* and *y*, as a function of the relative sizes and relative percentage uncertainties of *x* and *y*.

$$\sigma_F^{\%} = \left[\frac{x^2}{F^2}\sigma_x^{\%2} + \frac{y^2}{F^2}\sigma_y^{\%2} + \ldots\right]^{1/2} \quad (23)$$

This has some surprising results. To illustrate this, consider a simple example where F is a sum of just two variables, x and y. The percentage uncertainty in x is defined to be $\sigma_x^{\%} = \alpha$, and the percentage uncertainty in y, $\sigma_y^{\%} = K\alpha$, where K is the uncertainty ratio between the two variables. Equation (23) then becomes

$$\sigma_F^{\%} = \frac{\alpha}{F}\left(x^2 + K^2y^2\right)^{1/2} \quad (24)$$

Figure 24 shows $\sigma_F^{\%}$ (y-axis), normalised by α, as a function of the relative size of the two variables (x-axis), for a range of values of K (individual lines). The limits of the x-axis at 0 and 1 correspond to $x=0$ and $y=0$. At these limits the uncertainty $\sigma_F^{\%}$ tends towards the uncertainty in the dominant variable—$\sigma_y^{\%}$ and $\sigma_x^{\%}$ respectively. This is a logical result.

In the case where $K=1$ ($\sigma_x^{\%} = \sigma_y^{\%} = \alpha$), the uncertainty in F is lower than that in the input variables, for any relative size $x/(x+y)$. That is, $\sigma_F^{\%} < \alpha$. For $x/(x+y)=0.5$, $\sigma_F^{\%} = 0.7\alpha$, a 30% reduction compared to the underlying uncertainties. This effect is explained by the fact that the measurement errors in the two variables are assumed uncorrelated. As K is increased, the range of $x/(x+y)$ over which the uncertainty in the summation is less than α is reduced but does not entirely disappear. This leads to the counter-intuitive result that adding a very small proportion of

a comparatively high uncertainty component, y, to a dominant and lower uncertainty component, x, has the effect of *reducing* the uncertainty in the summed quantity.

In this paper, the application of the unsteady mass flow rate correction and the combination of the individual stream capacity terms to determine the overall vane capacity are practical examples of this effect. Consider the unsteady correction for the hub coolant stream. Here, x is the uncorrected mass flow, $x = \dot{m}_{\mathrm{h}} = 0.561\,\mathrm{kg\ s^{-1}}$, and y is the correction term, $y = \dot{m}''_{\mathrm{h}} = 0.002\,\mathrm{kg\ s^{-1}}$. Therefore, $x/(x+y) = 0.996$. The uncertainties in x and y are $\pm 0.703\%$ and $\pm 16.03\%$, respectively, giving $K \approx 22$. Applying equation (24), the resulting uncertainty in the summation value (corrected mass flow) is 0.9997α—that is, a reduction of 0.027%. This drop is very marginal, but illustrates how a counter-intuitive result can arise.